

Compressed Sensing for Time-Frequency Gravitational Wave Data Analysis

Paolo Addesso, Maurizio Longo, Stefano Marano, Vincenzo Matta
*Dept. of Electrical and Computer Engineering and Applied Mathematics,
University of Salerno, 84084 Fisciano (SA), Italy*

Maria Principe, Innocenzo M Pinto
*Waves Group, University of Sannio at Benevento,
82100 Benevento, Italy, INFN, LVC and KAGRA*
(Dated: March 7, 2022)

The potential of compressed sensing for obtaining sparse time-frequency representations for gravitational wave data analysis is illustrated by comparison with existing methods, as regards i) shedding light on the fine-structure of noise transients (glitches) in preparation of their classification, and ii) boosting the performance of waveform consistency tests in the detection of unmodeled transient gravitational wave signals using a network of detectors affected by unmodeled noise transients.

I. INTRODUCTION AND MOTIVATION

An important fraction of the Gravitational Wave (henceforth GW) signals of cosmic origin sought after by running and/or planned GW detection experiments based on optical interferometers [1]-[4] consists of *transient* signals. These include, e.g., binary inspirals/mergers/ringdowns, and supernova outbursts.

Transient *disturbances* of instrumental and/or enviromental origin, globally nicknamed *glitches*, are also ubiquitously observed in the data of interferometric GW detectors, occurring with various amplitudes, shapes, and rates.

In view of the essentially *unmodeled* nature of transient GWs of astrophysical interest [5], it is challenging to get rid from glitches. The problem is further complicated by the fact that glitches infringe the additive Gaussian stationary noise assumption on which most detection/estimation algorithms are based [6].

Substantial work has been made in GW experiments to understand the origin of glitches using additional information from environment and instrument monitoring channels, and to obtain reliable data quality assessment and vetoing criteria [7]-[9]. Consistency tests among the data gathered by several non co-located interferometers have been suggested and implemented to discriminate glitches, in view of their essentially *local* nature [10].

In the time-frequency (henceforth TF) domain, where non-stationary signals are most naturally represented [11], typical GW transients as well as typical instrumental glitches exhibit highly localized supports, and are thus technically *sparse*. GW chirps from inspiraling binary systems with large duration \times bandwidth figures are also sparse in the TF domain, yielding almost one-dimensional signatures (*ridges*), representing their instantaneous-frequency evolutions [12].

In the last few years a unifying conceptual framework for the efficient representation of sparse signals has been developed, globally referred to under the name of *compressed sensing* (henceforth CS). The power of the CS paradigm is witnessed by the exponentially growing scope of its applications (see, e.g., [13] for a broad and up to date list).

Using CS related concepts/tools in GW data analysis we may take advantage of the *sparsity* of both GW signals and instrumental glitches in the TF domain, for the purpose of i) enhancing the readability of TF representations of the data gathered by interferometric detectors, and ii) improving consistency tests among different detectors.

The potential of sparse representation for GW data analysis was independently recognized in [14] and [15], under a different perspective.

Our aim in this paper will be to illustrate by examples the potential of CS for TF GW data analysis, extending previous results in [16].

The paper is accordingly organized as follows. In Section II we review the key features of the relevant signal(s) and noise(s) and in Section III the basics of the TF representations referred to in the paper.

In Section IV we introduce sparse (skeletal) TF representations, and propose a CS-based algorithm for constructing them, together with pertinent implementation details.

In Section V we discuss a number of numerical experiments, where the proposed sparse TF representations are evaluated by comparison with other TF representation tools presently in use in GW data analysis. Conclusions follow under Section VI.

II. TRANSIENT GW SIGNALS AND GLITCHES

Transient GW signals can be represented in the form

$$s(t) = \text{Re}[\tilde{s}(t)], \text{ where } \tilde{s}(t) = S(t) \exp[i\psi(t)], \quad (1)$$

where the amplitude $S(t)$ function evolves adiabatically (i.e., on much longer timescales) compared to the phase $\psi(t)$, so that

$$\left| \frac{\dot{S}}{S} \right| \ll |\dot{\psi}|, \text{ and } \left| \frac{\ddot{\psi}}{\dot{\psi}^2} \right| \ll 1. \quad (2)$$

GW signals emitted by compact binary systems during their inspiral [17], merger [18], and ringdown [19] phase, as well as supernova core-collapse GW waveforms [20] belong to the above class.

The data gathered by interferometric GW detectors are embedded in additive noise. Once all narrowband features (power lines, natural-modes of the test-mass suspending wires, etc.) have been subtracted, the residual noise floor is found to consists of a locally-stationary, zero mean, coloured Gaussian random process $n(t)$, and a generalized impulsive component $g(t)$. This latter is basically a (random) superposition of transients of environmental/instrumental

origin (known as *glitches*), viz. [21]:

$$g(t) = \sum_{k=1}^K \psi_k(t), \quad (3)$$

K being the (random) number of such transients in the observation time-window, and $\psi_k(\cdot)$ the (random) glitches therein.

Transient GWs as well as glitches are typically *highly localized* in the TF plane, their support being restricted to tiny *spots* or narrow *stripes*.

III. TIME-FREQUENCY REPRESENTATIONS

Time-frequency representations provide the most natural framework for representing non stationary (transient) signals. A variety of different TF representations have been proposed, mostly in the XX century [22]-[26].

Several have been suggested or used for GW data analysis, including the linear short-time-Fourier, wavelet and constant-Q transforms (shortly reviewed in Sections III B-III D), the bilinear Bertrand [27] and Wigner-Ville (section III E) transforms, and the special (sparse) decompositions named after Hilbert-Huang (Section III F) and Mallat-Zhang (Section III G).

More exist, including the bilinear hyperbolic [28], higher-order (e.g., generalized Cohen-class [29], L-Wigner [30], polyspectral [31], polynomial [32]), and positive-definite [33] TF representations, that haven't been used so far in GW data analysis, to the best of our knowledge.

A. Time-Frequency Duality

Time-frequency duality (also known as the Gabor-Heisenberg principle) expresses the well known fact that the wider the time-support of $x(t)$, the narrower its frequency-support, and vice-versa. This property, that plays a key role in TF data analysis, can be formalized by introducing the time and frequency *barycenters*

$$t_0 = \int_{-\infty}^{+\infty} t |x(t)|^2 dt, \quad f_0 = \int_{-\infty}^{+\infty} f |X(f)|^2 df, \quad (4)$$

and the related *spreads* $\delta_t^{(x)}$ and $\delta_f^{(x)}$,

$$\delta_t^{(x)} = \left[\int_{-\infty}^{+\infty} (t - t_0)^2 |x(t)|^2 dt \right]^{1/2}, \quad \delta_f^{(x)} = \left[\int_{-\infty}^{+\infty} (f - f_0)^2 |X(f)|^2 df \right]^{1/2}, \quad (5)$$

$x(t)$ and $X(f)$ being a generic time function and its Fourier transform, yielding [11]

$$\delta_t^{(x)} \delta_f^{(x)} = \xi_x \geq (4\pi)^{-1}. \quad (6)$$

The quantity ξ_x depends on the chosen x function, is known as its TB (time-bandwidth) product, and attains its lower bound when $x(t)$ is a (unit-norm) Gabor function

$$x(t) = \frac{1}{\sqrt[4]{2\pi[\delta_t^{(x)}]^2}} \exp(-2\pi i f_0 t) \exp \left[-\left(\frac{t - t_0}{2\delta_t^{(x)}} \right)^2 \right]. \quad (7)$$

B. Short Time Fourier Transform

The short-time Fourier transform (STFT) is likely the simplest and oldest TF representation, and is defined by:

$$\mathcal{F}_x^{(h)}(t, f) = \int_{-\infty}^{+\infty} x(\tau) h(t - \tau) \exp(-2\pi i f \tau) d\tau \quad (8)$$

where $h(t)$ is a time-windowing function which vanishes for $|t| > \delta_t^{(h)}$. The STFT is the projection of $x(t)$ into an analyzing function whose envelope is a time-shifted version of $h(\tau)$ centered at $\tau = t$, whose (complex) carrier has frequency f . The (squared) modulus of the STFT, known as *spectrogram*,

$$S_x^{(h)}(t, f) = \left| \mathcal{F}_x^{(h)}(t, f) \right|^2 \quad (9)$$

has been frequently used as a fiducial representation of the frequency-distribution of signal energy for non-stationary signals. The frequency resolution of the STFT (and spectrogram) is the same for *all* f . Time-frequency duality implies that smaller values of $\delta_t^{(h)}$ (yielding larger time localization) entail poorer frequency resolution.

C. Wavelet Transform

The wavelet transform (WT) is defined by:

$$\mathcal{D}_x^{(h)}(t, f) = \left(\frac{f}{f_h} \right)^{1/2} \int_{-\infty}^{+\infty} x(\tau) h^* \left[\frac{f}{f_h} (t - \tau) \right] d\tau. \quad (10)$$

Here $h(t)$ is a zero-mean complex-valued time-windowed oscillatory function whose absolute Fourier spectrum is unimodal and peaked at $f = f_h$, known as *mother wavelet*, viz.,

$$h(t) = w(t) \exp(-2\pi i f_h t), \text{ where } w(t) = 0, \forall |t| > \delta_t^{(w)}. \quad (11)$$

It is seen that the wavelet transform is the projection of $x(\tau)$ into an analyzing function obtained by time-shifting the mother wavelet (from $\tau = 0$ to $\tau = t$), and *time-scaling* it via the frequency-dependent factor $a = (f/f_h)$ (which entails frequency-shifting its carrier from f_h to f).

Depending on whether $a \leq 1$, the above time-scaling corresponds to *time-squeezing* or *time-stretching*, and at the same time, in view of TF duality, to *frequency-stretching* or *frequency-squeezing*, respectively, by the same factor a . The (squared) modulus of the WT, known as *scalogram*,

$$\Sigma_x^{(h)}(t, f) = \left| \mathcal{D}_x^{(h)}(t, f) \right|^2 \quad (12)$$

can be used as a fiducial representation of the TF distribution of signal energy. We note in passing that both the spectrogram (9) and the scalogram (12) are unitary representations, i.e., satisfy signal energy conservation (Parseval theorem), viz.,

$$\int_{-\infty}^{+\infty} |x(\tau)|^2 d\tau = \int_{-\infty}^{+\infty} dt \int_{-\infty}^{+\infty} df S_x^{(h)}(t, f) = \int_{-\infty}^{+\infty} dt \int_{-\infty}^{+\infty} df \Sigma_x^{(h)}(t, f). \quad (13)$$

D. Q-Transform

As noted above, the STFT (and the spectrogram) is a *constant-bandwidth* representation, where the analyzing function duration (and bandwidth) is *the same* for all (t, f) . In the WT (and the scalogram), on the other hand, the effective time-width δ_t of the analyzing function at f is inversely proportional to f , and hence (in view of Gabor-Heisenberg theorem) the spectral-width δ_f is proportional to f , so that the ratio f/δ_f is *the same* for all f . Hence, the WT (and the scalogram) are basically *constant-Q* representations, Q being the name given to the f/δ_f ratio.

A different, but closely related, constant-Q TF representation is obtained by starting from the STFT, eq. (8), and letting the time-width of the windowing function to be inversely proportional to f , viz.:

$$\delta_t = \frac{C}{f} \quad (14)$$

so that, in view of TF duality

$$\delta_f = \frac{\xi}{\delta_t} = \frac{f\xi}{C} \quad (15)$$

yielding

$$\frac{f}{\delta_f} =: Q = \frac{C}{\xi}. \quad (16)$$

Under this assumption, equation (8) yields the so called *constant-Q transform* (henceforth QT),

$$\mathcal{Q}_x^{(h)}(t, f; Q) = \int_{-\infty}^{\infty} x(\tau) h_Q(t - \tau; f) \exp(-i2\pi f\tau) d\tau \quad (17)$$

where, denoting as $h(t)$ a chosen windowing function with time width $\delta_t^{(h)}$ and TB figure ξ_h ,

$$h_Q(t - \tau; f) = h \left[\frac{f\delta_t^{(h)}}{Q\xi_h}(t - \tau) \right]. \quad (18)$$

The form of eq. (17) suggests a convenient way for its computation, via a sequence of Fourier transforms (denoted below by the \mathcal{F} operator), viz.:

$$\mathcal{Q}_x^{(h)}(t, f; Q) = \mathcal{F}_{\xi \rightarrow t}^{-1} [X(\xi, f) H_Q^*(\xi; f)] \quad (19)$$

where,

$$X(\xi, f) = \mathcal{F}_{t \rightarrow \xi} [x(t) \exp(-i2\pi ft)], \quad (20)$$

and

$$H_Q(\xi, f) = \mathcal{F}_{t \rightarrow \xi} [h_Q(t; f)]. \quad (21)$$

The QT tiles the TF plane linearly in time and logarithmically in frequency, as shown in Figure 1, by comparison with the STFT and WT. In exploratory TF data analysis, the QT is usually computed for a set of (logarithmically-spaced) Q values, lower (higher) Qs yielding lower (higher) resolution in frequency, and higher (lower) resolution in time. The QT was introduced and developed in [36], [37], and was proposed as a tool for GW data analysis in [38], [39], leading to several currently perused implementations in LIGO-Virgo, including the the *Q*, *Omega*, and *Omicron* pipelines [38]-[40].

E. Wigner-Ville Transform

The Wigner-Ville (henceforth WV) transform of a real valued signal $x(t)$ reads [41]:

$$W_x(t, f) = \int_{-\infty}^{+\infty} \tilde{x}\left(t + \frac{\tau}{2}\right) \tilde{x}^*\left(t - \frac{\tau}{2}\right) e^{-i2\pi f\tau} d\tau \quad (22)$$

where $\tilde{x}(t)$ is the analytic mate of $x(t)$,

$$\tilde{x}(t) = x(t) + i\mathcal{H}[x(t)], \quad (23)$$

$\mathcal{H}[\cdot]$ denoting the Hilbert transform operator,

$$\mathcal{H}[x(t)] = \frac{1}{\pi} \oint_R \frac{x(\tau)}{t - \tau} d\tau = \mathcal{F}^{-1} \{U(f)\mathcal{F}[x]\} \quad (24)$$

where $U(\cdot)$ is Heaviside's step function.

Using the WV has been suggested for different purposes in GW data analysis, including the detection of GW chirps from inspiraling binaries, [42]-[44], and the estimation of GW arrival time-delays in a network of detectors for source localization [45].

The WV has a number of nice (and unique) properties [11] among all time-frequency representations: it is a member of the Cohen Class (i.e., it is covariant with respect to time and/or frequency shifts of its argument); its time (frequency) barycenter at fixed frequency (time) reproduce (and define) the group-delay and instantaneous frequency

of its argument; its marginal distribution along any radial line in the TF plane yields the energy density of the corresponding fractional Fourier transform [46], [47]. The WV is also *unitary*, i.e. energy preserving (Moyal theorem),

$$\left[\int_R |\tilde{x}(t)|^2 dt \right]^2 = \iint_{R^2} |W_x(t, f)|^2 dt df \quad (25)$$

and invertible (up to an irrelevant complex factor):

$$\tilde{x}(t) = \frac{1}{\tilde{x}^*(0)} \int_{-\infty}^{\infty} W_x(t/2, f) \exp(2i\pi ft) df. \quad (26)$$

The main limitation of the WV stems from its bilinear nature, entailing in general the appearance of intermodulation artifacts, which hinder its visual readability. The WV transform is immune from such artifacts only in two special cases, namely, when $x(t)$ is either a single noise-free constant-amplitude chirp whose frequency changes *linearly* with time, or a single noise-free Gabor (sine-Gaussian) function [41].

Different strategies have been proposed to get rid of the WV intermodulation artifacts, such as smoothing kernels [?] and reassignment [49], that are briefly discussed below.

1. Smoothed WV

The 2D Fourier transform of the Wigner-Ville distribution

$$A_x(\xi, \eta) = \mathcal{F}_{\substack{t \rightarrow \xi \\ f \rightarrow \eta}} [W_x(t, f)] \quad (27)$$

is known as the Ambiguity (or Woodward) Function (henceforth AF) of x , and the (ξ, η) plane is referred to as the AF domain, the ξ and η arguments being referred to as the Doppler-shift [sec^{-1}] and the delay [sec].

Interference artifacts in the WV exhibit rapid variations in the TF plane. Accordingly, they map far away from the origin in the AF plane, and can be effectively suppressed by multiplying the AF by some low-pass 2D-window function $\Lambda(\xi, \eta)$ vanishing beyond some distance from the origin of the AF plane, and transforming the windowed AF back to the (t, f) domain.

Multiplication in the (ξ, η) domain corresponds to convolution in the (t, f) domain (Borel theorem), and the resulting smoothed WVD can be written:

$$W_x^{(\lambda)}(t, f) = \iint_{R^2} W_x(\tau, \eta) \lambda(t - \tau, f - \nu) d\tau d\nu \quad (28)$$

where $\lambda(t, f)$ is the inverse Fourier transform of the 2D-windowing factor $\Lambda(\xi, \eta)$ in the AF domain, and is referred to as *smoothing kernel*. Smoothing (low pass filtering) of the WV entails some loss in its TF resolution.

It is worth noting that both the spectrogram (9) and the scalogram (12) are special smoothed versions of the WV, where the smoothing kernel $\lambda(t, f)$ is the WV transform of the pertinent windowing functions h in eqs. (8) and (10) [?].

Several smoothing kernels have been proposed, featuring different properties [48]r. In a series of papers [50]-[51] Baraniuk and Jones, developed the idea of seeking a radially-Gaussian windowing function in the AF plane, often referred to as radially Gaussian kernel (RGK) in the technical Literature, tailored to the actual energy distribution in the AF plane. They accordingly use polar coordinates (r, θ) in the AF plane, and let

$$K(r, \theta) = \exp \left[-\frac{r^2}{2\sigma^2(\theta)} \right] \quad (29)$$

where, in view of the AF symmetry property $A_x(-\xi, -\tau) = A_x(\xi, \tau)$,

$$K(r, \theta + \pi) = K(r, \theta), \quad (30)$$

and seek $\sigma(\theta)$ so as to maximize the energy content of the kernel-weighted AF

$$\int_0^{2\pi} d\theta \int_0^\infty r dr |A_x(r, \theta) K(r, \theta)|^2 \quad (31)$$

subject to a measure (area) constraint:

$$\int_0^{2\pi} d\theta \int_0^\infty r dr |K(r, \theta)|^2 \leq \alpha. \quad (32)$$

The Baraniuk-Jones radially Gaussian kernels are quite effective in producing intermodulation-artifact free smoothed versions of the WV, with nicely limited (and uniform) loss in TF resolution. The RGK smoothed version of the WV will be referred to as BJ-smoothed WV in the rest of this paper.

2. Reassignment

Reassignment is, basically, a heuristic procedure for *re-focusing* the WV, after it was blurred by smoothing, and can be understood without referring to a particular smoothing kernel [49].

According to (28), the value of the smoothed WV at any given point (t, f) is a weighted sum of all W_x values throughout the TF plane, the weighting factor being represented by the function $\lambda(\cdot, \cdot)$ centered in (t, f) .

Following Flandrin (who re-discovered and elaborated the reassignment concept introduced in [52]), "it is as if the total mass of an object were assigned to its geometric center - which is incorrect, except in the special case of *homogeneous density*". Reassignment accordingly consists in computing the TF coordinates of the *centroid* of W_x , as weighted by the (t, f) -centered $\lambda(\cdot, \cdot)$, viz.:

$$\hat{t}_x^{(h)} = \frac{\iint_{R^2} \tau W_x(\tau, \eta) \lambda(t - \tau, f - \nu) d\tau d\nu}{\iint_{R^2} W_x(\tau, \eta) \lambda(t - \tau, f - \nu) d\tau d\nu}, \quad (33)$$

$$\hat{f}_x^{(h)} = \frac{\iint_{R^2} \nu W_x(\tau, \eta) \lambda(t - \tau, f - \nu) d\tau d\nu}{\iint_{R^2} W_x(\tau, \eta) \lambda(t - \tau, f - \nu) d\tau d\nu} \quad (34)$$

and *reassigning* the value of the WVD originally computed in (t, f) to the point $(\hat{t}_x^{(h)}, \hat{f}_x^{(h)})$. Reassignment performs very well in the absence of noise.

F. Hilbert-Huang-Transform

The Hilbert-Huang-Transform (henceforth HHT), consists of two steps. The first one, known as Empirical Mode Decomposition (EMD) [53], is a constructive recipe for adaptively representing a nonstationary signal as

$$S(t) = \sum_{k=1}^N s_k(t) + r(t) \quad (35)$$

where $r(t)$ is a *monotonic* (possibly null) residual, and the *intrinsic mode functions* (IMF) $s_k(t)$ are obtained by an exhaustive *sifting* procedure, consisting in defining the functions

$$m_{h-1}(t) = \begin{cases} S(t), & h = 1, \\ S(t) - \sum_{k=1}^{h-1} s_k(t), & h > 1, \end{cases} \quad (36)$$

computing their *mean-envelope* μ_{h-1} (average of upper and lower envelopes), and letting

$$s_h = m_{h-1} - \mu_{h-1}. \quad (37)$$

As shown in [54], EMD attempts (and often succeeds) identifying the various scales at which a signal oscillates, in a fully data-driven way. Indeed, the IMF spectra organize spontaneously as an almost constant-Q dyadic wavelet-like filter bank [55].

In the second step, the analytic mate of *each* IMF is constructed via the Hilbert transform (HT),

$$\tilde{s}_k(t) = A_k(t) \exp[i\psi_k(t)] = s_k(t) + i\mathcal{H}[s_k(t)] \quad (38)$$

whereby an instantaneous amplitude $A_k(t)$ (henceforth IA) is associated to a fiducial *instantaneous angular frequency* $\dot{\psi}_k(t)$ (henceforth IF), computed from the (numerical) time-derivative of the instantaneous phase $\psi_k(t)$. This yields the Hilbert spectrum, aka the HHT:

$$H_S(t, \omega) = \frac{1}{2\pi} \sum_k A_k(t) \delta \left[f - \frac{\dot{\psi}_k(t)}{2\pi} \right] \quad (39)$$

whereby each IMF is represented by a 1D feature in the TF plane (its fiducial instantaneous-frequency line, henceforth IFL), whose points have different levels, given by the pertinent IA.

The HHT was introduced in GW data analysis in [56], and further exploited in [57]. A recent review of the related implementation aspects can be found in [58].

Note that the Hilbert spectrum (39) holds no information about the instantaneous bandwidth (IBW) of the signal [59]-[61]. An IBW-aware version of the HHT can be obtained in principle by estimating the IBW at each point (time) along the IFL, and re-distributing the local energy (squared IA) over an IBW-wide frequency interval, according to some suitable/fiducial fall-off law.

The original EMD method lacks a rigorous mathematical foundation, and hence its convergence properties, and resilience against noise are not well established [53].

In principle, it should be noted that any given (smooth, limited) signal $x(t)$ can be represented by an *infinite* number of possible $\{a(t), \phi(t)\}$ pairs such that $x(t) = a(t) \cos[\phi(t)]$ (see, e.g., [62] for a general discussion, and [63] for simple examples). In addition, the HHT algorithm is based on the assumption that $\mathcal{H}[A(t) \cos[\psi(t)]] = A(t) \sin[\psi(t)]$, which holds only if i) the Fourier spectra of the envelope $A(t)$ and carrier $\cos[\psi(t)]$ do not nonoverlap [65], and ii) $H[\cos[\psi(t)]] = \sin[\psi(t)]$, which is (asymptotically) true under broad but *not* completely general assumptions [66].

A mathematically sound (and better performing, e.g., in the case of multi-tone signals) EMD-like algorithm, known as the synchro-squeezed wavelet transform was introduced in [67].

Conceptual as well as technical (implementation) issues also exist as regards both the EMD and the HT steps of the HHT algorithm:

- In the original EMD algorithm [53] spline-fitting is used to construct the upper/lower waveform envelopes, at each step of the sifting procedure. This choice entails the appearance of end-point over/undershoot, that may hinder faithful IMF recovery. Alternative EMD algorithms (based on constrained optimization, rather than spline-fitting) have been proposed to circumvent this problem [68]. Mode mixing, whereby a single IMF may include different signal components, or a single component may be split across several IMFs is another known issue. Modified EMD algorithm have been used to mitigate this problem, the key idea being that of averaging different IMFs obtained by applying EMD to several superpositions of the signal with different (independent) realizations of noise [69]. Better IMF reconstruction has been achieved using wavelet-based projections using the Fejer-Korovkin class of wavelet filters [70].
- The Hilbert Transform step is usually implemented via (fast) discrete Fourier transform (DFT), and is accordingly affected by spectral leakage and distortion, which may spoil the subsequent IF estimation. Numerical differentiation used to retrieve the instantaneous frequency is, in addition, quite sensitive to noise. Alternatives to the DFT-HT have been suggested to fix these limitations, with partial success (e.g., interpolative approaches to retrieve the IAs [71], and 1st-order autoregressive modeling for estimating the IFs [72]).

None of the above HHT improvements has been applied, to the best of our knowledge, in GW data analysis so far. The most serious limitation of the HHT lies in its *limited* frequency-resolution (in contrast to claims made in [56]-[58]). Indeed, as shown in [73], a signal consisting of two (pure) tones, will *not* be solved by the HHT, if the frequency difference does not exceed a *confusion bandwidth* depending on the ratio between the amplitudes of the two tones [74]. An improved EMD algorithm with tunable frequency resolution was proposed in [75].

In [?] the EMD was used, to derive a set of ambiguity-domain smoothing filters (one for each IMF) whereby different "views" of the WV of the original signal could be obtained, and combined to give a TF representation referred to as EMD-smoothed WV.

G. Atomic Decompositions

Mallat and Zhang are credited for inventing the matching-pursuit algorithm [77] for decomposing a signal into elementary transients, represented by Gabor atoms [78], [79].

The analytic mate of a SG (Gabor) atom $s(t)$ can be approximated by

$$\tilde{s}(t) = a(t) \exp[i\phi(t)], \quad (40)$$

with

$$a(t) = A_0 \exp\{-(t-t_0)/\Delta T\}^2, \quad \phi(t) = 2\pi f_0 t + \psi, \quad (41)$$

provided the product between the SG *carrier* frequency f_0 and time-spread ΔT is large ($\gg 1$). The BT figure of Gabor atoms attains the minimum value allowed by time-frequency duality for any values of the atom parameters, and the WV transform of the SG-Gabor atom (41) is real and positive,

$$W_{\tilde{s}}(t, f) = \Delta T \sqrt{2\pi} A_0^2 \exp\{-2[(t-t_0)/\Delta T]^2\} \exp\{-2\pi^2[(f-f_0)\Delta T]^2\}. \quad (42)$$

Adding the WVs of the *individual* atoms in the AD yields a sparse, intermodulation artifact-free, fiducial energy-distribution of the signal in the TF domain, known as *W(i)V(i)gram* [77].

The AD concept was introduced in GW data analysis in [21] with reference to glitches, and further pursued in [80], [81]. Under the name of Sine-Gaussians (henceforth SG), Gabor atoms have been also used to represent generic GW bursts [82].

It should be noted that ADs are *non-unique*, the choice of the atoms being largely arbitrary. Alternative atom choices include, e.g., exponentially damped sinusoids [83], and modulated Gamma-envelopes [84].

The physical readability of atomic representations is strongly affected by the choice of the atoms, and this ultimately leads to the problem of finding the atoms which are the most *natural* choice for the signals being analyzed [85].

MP-derived ADs may display *strong* atoms in time intervals where the original signal is *negligibly small*. These atoms usually *cancel out* in the reconstructed waveform by destructive interference, but stand out in the WiVigram (due to the positive sign definiteness of 42). Pictorially, such atoms are said to form the *dark energy* of the AD [86].

Modified MP algorithm have been proposed attempting to minimize not only the reconstruction energy (L^2) error, but also its dark-energy content [87], [88].

IV. FROM WV TO TF SKELETONS VIA CS

The TF representation of the data gathered by an interferometric GW detector contains (noise-blurred) *sparse* features. These include highly localized *juts*, representing glitches and GW transients with small time-bandwidth figures, and *ridges*, i.e. almost one-dimensional features representing the frequency evolution of wideband GW chirps. Together, the above sparse features form the (generalized) TF *skeleton* of the data.

Unfortunately, *no* TF representation (including the WV, wavelet and Q transform) returns the skeleton of the data. The AD and HHT attempt to find sparse TF approximations consisting only of "juts" or "ridges", respectively. This is physically unjustified, and limits their range of meaningful applicability.

In this section we use the compressed sensing paradigm to derive general, *sparse* and *highly resolved* TF representations from the WV without making any unjustified assumption, following the approach originally proposed in [91].

As shown in [91], this technique compares favorably to [?]–[49] in terms of effectiveness and computational burden. It is worth stressing, however, that it does not attempt to derive an artifact-free WV representation, but rather to *construct the skeleton* of the TF distribution which is a-priori unknown, and otherwise unavailable.

The CS paradigm relies on the fact that signals that are sparse in the TF domain can be essentially recovered using a relatively *small* set of samples from the Fourier-*conjugate* domain, where the signal is expected to be *dense*, according to the Gabor-Heisenberg principle [92], [93].

To exploit this property, we start from the AF :

$$A_x(\xi, \tau) = \mathcal{F}[W_x(t, f)] \quad (43)$$

and manage to distill the (sparsest) TF representation (skeleton) of our data using a bunch of values of the AF from a suitable neighbourhood Ω of the origin in the (ξ, τ) plane. Doing so we use again the well known property of the WV representation whereby its highly-oscillatory intermodulation artifacts map *far away* from the origin in the AF plane .

Formally, we seek a *sparse* TF distribution $\widehat{\mathcal{W}}$ such that

$$\widehat{\mathcal{W}}(t, f) = \arg \min \|\mathcal{W}(t, f)\|_0 : S_\Omega(\xi, \tau) \{ \mathcal{F}[\mathcal{W}(t, f)] - A_x(\xi, \tau) \} = 0. \quad (44)$$

where the L_0 norm $\|\cdot\|_0$ is the cardinality of the (discrete) support of its argument, and

$$S_\Omega(\xi, \tau) = \begin{cases} 1, & (\xi, \tau) \in \Omega \\ 0, & (\xi, \tau) \notin \Omega \end{cases}. \quad (45)$$

The *cardinality* (size) and *shape* of Ω should be judiciously chosen for best performance, as further discussed in Section IV B.

A. Computational Cost and Practical Implementation

The optimization problem (44) is combinatorially complex, and thus almost unaffordable from a computational viewpoint. Remarkably, under fairly general conditions one can rather address the *viable* problem

$$\widehat{\mathcal{W}}(t, f) = \arg \min \|\mathcal{W}(t, f)\|_1 : S_\Omega(\xi, \tau) \{\mathcal{F}[\mathcal{W}(t, f)] - A_x(\xi, \tau)\} = 0 \quad (46)$$

where the L_1 norm has replaced the L_0 one [92]. In order to take into account the noisiness of the data it is further expedient to relax the equality constraint in (46), replacing it with a suitable bound on the error L_2 norm, viz.

$$\widehat{\mathcal{W}}(t, f) = \operatorname{argmin} \|\mathcal{W}(t, f)\|_1 : \|S_\Omega(\xi, \tau) \{\mathcal{F}[\mathcal{W}(t, f)] - A_x(\xi, \tau)\}\|_2 \leq \epsilon. \quad (47)$$

The optimization problem (47) can be implemented in several ways, including, e.g., log-barrier, interior-point and iteratively-reweighted least-squares algorithms, whose implementations and computational costs have been discussed in [94], [95], [96], respectively.

Convex analysis also tells us that any nontrivial solution of (47) is also a solution of

$$\widehat{\mathcal{W}}(t, f) = \operatorname{argmin} \lambda \|\mathcal{W}(t, f)\|_1 + \frac{1}{2} \|S_\Omega(\xi, \tau) \{\mathcal{F}[\mathcal{W}(t, f)] - A_x(\xi, \tau)\}\|_2^2 \quad (48)$$

for *some* $\lambda > 0$, as shown, e.g., in [97]. In [98] a class of numerically efficient algorithms is proposed for solving (48), which are computationally cheaper than solving (47) directly. As noted in [98], a sensible choice for λ is

$$\lambda = \gamma \|\mathcal{F}^{-1}[\Omega A_x]\|_\infty, \quad \gamma \sim 0.1 \quad (49)$$

typically yielding $\epsilon \sim 10^{-2}$ in (47) in our numerical experiments, which is adequate for our present purposes.

B. Choice of the Ω Domain

The choice of the *cardinality* (number of TF samples) and *shape* of Ω , affects the skeleton appearance in rather subtle ways, depending on the features of the signals.

As the cardinality (hence the diameter) of Ω increases, we may expect more and more intermodulation products to appear in \mathcal{W} , until eventually the whole WV distribution is recovered in the limit where Ω covers the whole TF plane. On the other hand, as the cardinality of Ω is decreased, we expect the skeletal components to be gradually spoiled.

In [91] a number of multicomponent signals with *known* skeletons was considered, and it was shown that for a WV of size $N \times N$, the choice $\operatorname{card}[\Omega] \sim N$ (the Heisenberg-Gabor cardinality) was the best one [99]. However, as noted in [91], for a given cardinality N , a better skeleton reconstruction is obtained if the *shape* of Ω *fits* the shape of the ambiguity function, reflecting the *coherency* properties of the signal.

In this connection it would be desirable to find a systematic and, as far as possible, *non*-parametric procedure, to determine the shape of Ω .

We adopted a simple (and rather natural) choice for Ω , namely the domain whose boundary $\partial\Omega$ is the contour level of the RGK (29) embracing N samples of the AF. As we shall see, this choice yields a more faithful representation of the skeleton, in all cases where this latter is known a priori, compared to the *isotropic* domain [90] suggested in [91]. It is worth noting that in the present work, kernel adaptation and sparsity promotion are dealt with sequentially. Alternatively (and perhaps more efficiently) [100], the function $\sigma(\theta)$ in eq. (29) can be sought as part of the solution of the sparsification problem (44).

V. NUMERICAL EXPERIMENTS

In this section we manage to illustrate by numerical simulations how CS-based TF skeleton representations may offer sharper time-frequency resolution (which is important for classifying glitches and understanding their origin) and substantial de-noising (which is important for detection purposes). A deeper analysis, in particular as regards the statistical properties of these representations, will be the subject of future work.

In our numerical experiments, the domain Ω was determined as discussed in Section IV B, using the public-domain RGK toolbox [101]. The gradient projection algorithm proposed in [98], from the public-domain GPSR toolbox [102] was used to solve the optimization problem (48), using eq. (49) for the parameter λ . All waveforms were sampled at 1 KHz in chunks 512 samples wide, unless otherwise stated. Q-transforms were computed using the toolbox from [103], and HHT transforms were computed using public domain codes from the Mathworks repository.

A. Gabor Molecules

Simple Gabor molecules, consisting of two SG waveforms (Gabor atoms) are perhaps the simplest *multicomponent* transient signals, and provide a convenient elementary benchmark for a preliminary, controlled comparison among different TF representations. Here, following [104], we content ourselves with an operational definition of a multicomponent transient, as a signal whose TF skeleton consists of *separate* features, i.e., blobs or ridges whose TF supports exhibit the property that their frequency (time) separation at all times (frequencies) is larger than the sum of their local frequency (time) spreads.

The panels in first (leftmost) column of Figs 2-4 display (from top to bottom) the time domain data, frequency spectrum, and fiducial TF skeleton, which can be computed explicitly from the WV, in this case, by subtracting the intermodulation terms.

The second column (from left to right) shows the three visually best Q-transforms (in a range of Q values between 5 and 50).

The next (third) column shows the WV distribution, the BJ-smoothed WV, and the CC skeleton computed using the optimized Ω domain.

Finally, the two panels in the fourth and last column display the HHT transform, and its plain (top panel) and IBW-aware (bottom panel, here nicknamed *fat*) versions. We used eq. (17) from [105] to estimate the IBW and construct the IBW-aware version of the HHT, assuming the (instantaneous) amplitude to fall off linearly from a maximum at the IF, down to zero at the half-bandwidth edges, while keeping the total energy (integral of squared instantaneous amplitude across the IBW) equal to the squared IA of the original HHT.

In Fig. 2 the molecule consists of two SG having the same time width, but different time centroids, carrier frequencies and peak amplitudes; in Fig. 3 the two atoms have the same carrier frequency but different time centroids; in Fig. 4 they have the same time centroid but different carrier frequencies.

The CC skeleton computed using the optimized Ω domain yields the sharpest TF localization, and goes closest to the actual skeleton for all cases considered. The visually best Q-transform appears less well localized. The *fat* HHT also yields a sharp TF signature for the cases in Figures 2 and 3 - but in the case of atoms with coincident time-centroids and *close* carrier frequencies (Fig. 4), it fails to reproduce the actual skeleton, being fooled by the resulting beat.

Due to the noted limitation, and for the sake of conciseness, in the following Sections we will not include the HHT among the compared TF representations.

B. GW Transients and Glitches

The qualitative conclusions valid for Gabor molecules are essentially confirmed for realistic waveforms representing both sought GW transients and glitches of environmental/instrumental origin.

Figure 5 refers to a supernova core-collapse GW waveform from [20]. The sampling frequency is 16KHz in this case. Here again the TF skeleton obtained using the BJ-optimized Ω domain yields the best TF localization, followed by the BJ-smoothed WV. These two representations display sharp TF signatures of both the "bounce" component (the "blob") and the subsequent "ringdown" (the "ridge") in the signal. The Q-transforms are comparatively less sharp and more blurred, and show an evident tradeoff between time and frequency resolution, as the Q value is varied. The WV is heavily affected by signal-noise intermodulation artifacts.

Figures 6a-c display three prototypical glitches from the LIGO 5th Scientific Run, from [106] (more glitch skeletons are available in [107]). Here also the TF skeleton obtained using BJ-optimized Ω domain yields the sharpest TF localization. The BJ-smoothed WV comes next. The visually-best Q-transform appears to be close to the TF skeleton obtained using the square Ω domain.

The case of Fig. 6a, showing part of the filtered file #866273637 observed in the data channel (DARM_ERR) of LIGO-Hanford detector (H1) is particularly interesting. Its optimized TF skeleton (and BJ-smoothed WV) clearly show four elementary TF features ("blobs"), suggesting that this glitch is actually a *multicomponent* waveform (this is also confirmed by atomic decomposition).

In the case of the typical filtered power mains glitch sensed by an environmental magnetometer (LIGO POWMAG channel) shown in Fig. 6b all TF representations yield acceptable results, except the TF skeleton obtained using the square Ω domain. This is not surprising, given the highly anisotropic character of the AF in this case.

Figure 7 displays a typical "arch-shaped" glitch seen in the GEO-600 data [108]. Such glitches originate from scattered light where seismic motion modulates the scatterers' velocity, and hence represent nonlinear products of environmental noise. Also in this case, the TF skeleton obtained using the BJ-optimized Ω domain and the BJ-smoothed WV yield quite sharp TF distributions. The TF skeleton obtained using the square domain is on a par with the (visually best) Q-transform in terms of resolution, while looking less noisy compared to this latter.

C. TF Consistency Tests

Sparse representations are intrinsically denoising [92]. Accordingly we may expect that using TF skeletons may boost the performance of TF consistency tests among multiple detector data.

This is illustrated in Figs 8a to 8h. Here we assume for simplicity that the direction of arrival of the GWs is fiducially known from different (e.g., EM or neutrino) observations (triggered detection), and consider the following simplest TF-consistency test:

1. let W_m the TF representation (plain or BJ-smoothed WV, or TF estimated TF skeleton) built from the data gathered by the m -th receiver, $m = 1, 2, \dots, M$;
2. time-shift the TF representations by the appropriate (known) propagation delays;
3. compute the "coincidence" TF representation

$$W^{(c)}(t, f) = \left| \prod_{m=1}^M W_m(t, f) \right|^{1/M}; \quad (50)$$

4. define the pixels in the coincidence TF representation whose level is above the median as "hot".

In Figs 8a to 8h we restrict ourselves to the simplest 2-detectors case. In Figs 8a and 8b the data contain a GW chirp corrupted by glitches in additive white Gaussian noise. The SNR of the chirp against the Gaussian background is 15, and is twice that of the glitches. Figure 8a displays the WV, the BJ-smoothed WV and the TF skeleton (using the BJ-optimized Ω domain). Figure 8b displays the Q-transforms, for $Q = 8, 20.2$ and 32 . The panels in the bottom row of Fig. 8a and 8b show the coincidence TF distributions.

The intermodulation artifacts of the WV are evident in Fig. 8a, and impair its readability. The BJ-smoothed WV, and the TF skeletons in Fig. 8a, and the Q-transforms in Fig. 8b clearly show both the GW skeletons and the offending glitches. These latter disappear, as expected, in the coincidence representations. The TF skeleton exhibits the sharpest time-frequency localization, and also the largest contrast against the background, compared to both the BJ-smoothed WV and the Q-transforms, suggesting good denoising, further discussed in Sect. VD.

In Figs 8c and 8d the data contain a GW merger corrupted by glitches, in additive white Gaussian noise. The SNR of the merger against the Gaussian background is 10, and is twice that of the glitches. Figure 8c displays the WV, the BJ-smoothed WV and the TF skeleton (using the BJ-optimized Ω domain). Figure 8d displays the Q-transforms, for $Q = 8, 12.7$ and 20 . The panels in the bottom row of Fig. 8c and 8d show the pertinent coincidence TF distributions. Inspection of these figures leads to conclusions similar to those drawn from Figs 8a and 8b.

Finally, in Figs 8e and 8f the data consist of white Gaussian noise only. The BJ-smoothed WV and the Q-transforms exhibit some peculiar hot pixel patterns. The TF skeleton coincidence clearly features the lowest number of spurious hot pixels.

D. Coincidence TF Skeletons and Denoising

The nice properties of the coincidence TF skeleton in terms of denoising are illustrated in Figs 9a and 9b, showing the level histograms of the "hot" pixels drawn from the various coincidence TF representations discussed above. In

each histogram panel the number of hot pixels, their average level, and their cumulative level sum are displayed. In the WV, BJ-smoothed WV and Q-transform cases the number of hot pixels is one half the size of the corresponding (discrete) TF representations. The average level and cumulative level sum of the hot pixels for the two cases where a signal is present is only slightly larger (by a factor always < 2) compared to the case of noise only.

In the TF skeleton, as an effect of sparsification, the number of hot pixels is smaller by a factor $\sim 10^2$ compared to the size of the (discrete) WV. In the chirp case (with SNR=15) the energy content of the signal in the TF plane is spread along a ridge (consisting of $\sim 1.6 \cdot 10^3$ hot pixels, in our example) while in the merger case (with SNR=10) it is concentrated in a blob (consisting of $\sim 3 \cdot 10^2$ hot pixels, in our example). Compared to the case of noise only, the average level of the hot pixels is larger by a factor ~ 5 (for the chirp) and ~ 10 (for the merger), and the cumulative sum of the hot pixel levels is larger by a factor ~ 1.7 (for the merger) and ~ 4.5 (for the chirp).

The above suggests that TF based skeletonization has inherent denoising capabilities, and that the WV, the BJ-smoothed WV and the Q-transform have comparable performances in TF coincidence tests.

VI. CONCLUSIONS

We reviewed the compressed sensing (CS) paradigm, and suggested its possible use in TF GW data analysis, using illustrative examples. Gravitational wave chirps and bursts as well as instrumental glitches share the common feature of being represented by *sparse* TF objects, including thin $1D$ - ridges, and localized $2D$ - juts. The main goal of the TF skeleton construction algorithm is to produce readable TF representations of complex, sparse, multi-component waveforms, which are free from intermodulation artifacts and still offer as much time-frequency resolution as possible. These are *conflicting* requirements, nonetheless the WV-CS based approach yields an excellent tradeoff between them, as illustrated. We managed to show that TF skeletons may yield better insight into the *fine structure* of glitches, hopefully improving our understanding about their origin, and our skill in classifying them. We also showed that CS-based sparse TF representations (skeletons) act as an effective denoising algorithm, improving TF-based coincidence tests.

We accordingly suggest that sparse CS-based TF skeletons may be nice complements to existing tools for GW data analysis.

ACKNOWLEDGEMENTS

This work has been supported by the Italian Ministry for University and Scientific Research (MIUR) through the grant 20082J7FBN.

REFERENCES

-
- [1] <http://www.ligo.caltech.edu>
 - [2] <http://www.virgo.infn.it>
 - [3] <http://www.geo600.uni-hannover.de>
 - [4] <http://gwcenter.icrr.u-tokyo.ac.jp/en/>
 - [5] N. Anderson and K.D. Kokkotas, "Gravitational Wave Astronomy: the High Frequency Window," *Lec. Not. Phys.* **653** (2005) 255.
 - [6] M. Principe and I.M. Pinto, "Locally Optimum Network Detector of Unmodeled GW Bursts in Glitch Noise," LIGO-P1000134 (2010).
 - [7] L. Blackburn et al. "The LSC Glitch Group: Monitoring Noise Transients During the Fifth LIGO Science Run," *Class. Quantum Grav.* **25** (2008) 184004.
 - [8] N. Christensen et al., "LIGO S6 detector characterization studies," *Class. Quantum Grav.* **27** (2010) 194010.
 - [9] J.Aasi et al., "The Characterization of Virgo Data and its Impact on Gravitational-Wave Searches," *Class. Quantum Grav.* **29** (2012) 155002.
 - [10] N. Arnaud et al., "Coincidence and Coherent Data Analysis Methods for Gravitational Wave Bursts in a Network of Interferometric Detectors," *Phys. Rev.* **D68** (2003) 102001.
 - [11] L. Cohen, "Time-Frequency Distributions: a Review," *Proc. of the IEEE*, **77** (1989) 941.
 - [12] B. Boashash, "Estimating and Understanding the Instantaneous Frequency of a Signal - I," *Proc. IEEE* **80** (1992) 520.

- [13] The Rice University Compressive Sensing Resources page, <http://dsp.rice.edu/CS>
- [14] I.M. Pinto and V. Matta, "Sparse Representations for Detecting Unmodeled Transients and Representing Unmodeled Glitches," LIGO Document G1200986 (2012).
- [15] R. Inta, "Sparse Methods for Gravitational Wave Detection," LIGO document G1200593 (2012).
- [16] P. Addesso et al., "Sparsifying Time-Frequency Distributions for Gravitational Wave Data Analysis," Proc. 3rd IEEE Intl. Workshop on Compressed Sensing Th. Appl., Pisa (2015), p. 154.
- [17] L. Blanchet., "Gravitational Radiation from Post-Newtonian Sources and Inspiralling Compact Binaries," Living Rev. Gen. Relativity **9** (2006) 4.
- [18] J.G. Baker et al., "Comparison of Binary Black Hole Merger Waveforms," Class. Quantum Grav. **24** (2007) S25.
- [19] Th. Damour and A. Nagar, "New Analytic Representation of the Ringdown Waveform of Coalescing Spinning Black Hole Binaries," Phys. Rev **D90** (2014) 024054.
- [20] H. Dimmelmaier et al., "Gravitational Wave Burst Signals from Core Collapse of Rotating Stars," Phys. Rev. **D78** (2008) 064056.
- [21] M. Principe and I.M. Pinto, "Modeling the Impulsive Noise Component and its Effect on the Operation of a Simple Coherent Network Algorithm for Detecting Unmodeled Gravitational Wave Bursts," Class. Quantum Grav., **25**, 075013 (2008).
- [22] L. Cohen, *Time-Frequency Analysis*, Englewood Cliffs, NJ: Prentice- Hall, 1995.
- [23] P. Flandrin, *Time-Frequency/Time-Scale Analysis*, San Diego, CA: Academic, 1999.
- [24] S. G. Mallat, *A Wavelet Tour of Signal Processing*, New York: Academic, 1998.
- [25] B. Boashash, "Time-Frequency Signal Analysis and Processing," New York, Elsevier, 2015.
- [26] F. Hlawatsch and G. F. Boudreaux-Bartels, Linear and Quadratic Time Frequency Signal Representations, IEEE Signal Processing Mag., pp. 2167, Apr. 1992.
- [27] J. Bertrand and P. Bertrand, A Class of Affine Wigner Distributions with Extended Covariance Properties, J. Math. Phys., **33**, 2515 (1992).
- [28] A. Papandreou, F. Hlawatsch, and G. F. Boudreaux-Bartels, The Hyperbolic Class of QTFRs Part I: Constant-Q Warping, the Hyperbolic Paradigm, Properties, and Members, IEEE Trans. Signal Processing, **SP-41**, 3425 (1993).
- [29] P. O. Amblard and J. L. Lacoume, Construction of Fourth Order Cohens Class: a Deductive Approach, in Proc. IEEE Int. Symp. on TimeFreq. Time-Scale Anal., 1992, p. 257.
- [30] L. J. Stankovic, A Method for Improved Distribution Concentration in the Time-Frequency Analysis of Multicomponent Signals Using the L-Wigner Distribution, IEEE Trans. Signal Processing, **SP-43**, 1262 (1995).
- [31] J.R. Fonollosa, C.L. Nikias, "Wigner Higher Order Moment Spectra: Definition Properties, Computation and Applications to Transient Signal Analysis," IEEE Trans. **SP-41**, 245 (1993).
- [32] B. Boashash and P. OShea, Polynomial WignerVille Distributions and their Relationship to Time-Varying Higher Order Spectra, IEEE Trans. Signal Processing, **SP-42**, 216 (1994).
- [33] P. Loughlin, J. Pitton, and L. Atlas, Construction of Positive Time-Frequency Distributions, IEEE Transactions on Signal Processing **42**, 2697 (1994).
- [34] L. Blackburn, "KleineWelle Technical Document," LIGO Technical Note T060221-00-Z (2007); id. "Glitch investigations with Kleine Welle," LIGO Document G050158 (2005).
- [35] S. K. Chatterji, "Introduction to Q-Scan," LIGO Document G060483 (2006).
- [36] J.C. Brown, "Calculation of a Constant Q Spectral Transform," J. Acoust. Soc. Am., **89** (1991) 425.
- [37] J.C. Brown and M.S. Puckette, "An efficient Algorithm for the Calculation of a Constant Q Transform," J. Acoust. Soc. Am., **92** (1992) 2698.
- [38] S. K. Chatterji, "The Search for Gravitational-Wave Bursts in Data from the second LIGO Science Run," PhD thesis, MIT, Boston MA, USA (2003).
- [39] S. K. Chatterji et al., "Multiresolution Techniques for the Detection of GW Bursts," Class Quantum Grav. **21** (2004) S1809.
- [40] F. Robinet, "Omicron: an Algorithm to Detect and Characterize Transient Noise in Gravitational-Wave Detectors." <https://tds.ego-gw.it/ql/?c=10651> (2015).
- [41] T. A. C. M. Claassen and W. F. G. Mecklenbrauker, The Wigner Distribution-a Tool for Time-Frequency Signal Analysis, Philips J. Res., **35**, 217 (1980); *ibid.*, p. 276.
- [42] M. Feo et al "Efficient GW Chirp Detection and Estimation via Time-Frequency Analysis and Edge Detection," in *Proc. 7th Marcel Grossman Meeting on General Relativity*, R. T. Jantzen et al., Eds., Singapore: World Scientific, p 1086.
- [43] W. G. Anderson and R. Balasubramanian R, 1999 " Time-Frequency Detection of Gravitational Waves," Phys. Rev. **D 60** (1999) 102001.
- [44] E. Chassande-Mottin and P. Flandrin "On the Time-Frequency Detection of Chirps," Appl. Comp. Harm. Anal. **6** (1999) 252.
- [45] R.P. Croce et al., "Robust Gravitational Wave Burst Detection and Source Localization in a Network of Interferometers Using Cross-Wigner Spectra," Class. Quantum Grav. **19** (2011) 045001.
- [46] D. Mustard, "The Fractional Fourier Transform and the Wigner Distribution," J. Austral. Math. Soc., **B 38**, 209 (1996).
- [47] The equality between the time (frequency) marginal distribution of the WV and the power (spectral density) of its argument is a special case of the above property.
- [48] F. Hlawatsch et al., " Smoothed Pseudo Wigner Distribution, Choi-Williams Distribution and Cone-Kernel Representation: Ambiguity Domain Analysis and Experimental Comparison," Signal Processing **43** (1995) 149.
- [49] P. Flandrin, F. Auger, and E. Chassande-Mottin, "Time-frequency Reassignment: From principles to Algorithms," in

Applications in Time-Frequency Signal Processing, A. Papandreou-Suppappola, Ed., CRC Press, Boca Raton FL, USA (2003), ch. 5.

- [50] R.G. Baraniuk and D.L. Jones, "A Signal-Dependent Time-Frequency Representation: Optimal Kernel Design," IEEE Trans. **SP-41** (1993) 1589.
- [51] R.G. Baraniuk and D.L. Jones, "Signal-Dependent Time-Frequency Analysis using a Radially Gaussian Kernel," Signal Proc. **32** (1993) 263.
- [52] K. Kodera, C. De Villedary, and R. Gendrin, "A New Method for the Numerical Analysis of Nonstationary Signals," Phys. Earth Plan. Int., **12**, 142 (1976).
- [53] N.E. Huang, et al., "The Empirical Mode Decomposition and the Hilbert Spectrum for Nonlinear and Nonstationary Time Series Analysis," Proc. Roy. Soc., **A454**, 903 (1998).
- [54] P. Flandrin and P. Goncalves, "Empirical Mode Decomposition as Data-Driven Wavelet-like Expansion," Int. J. Wavelets, Multires. and Info. Proc, **2**, 1 (2004).
- [55] P. Flandrin, G. Rilling and P. Goncalves, "Empirical Mode Decomposition as a Filter Bank," IEEE Sig. Proc. Lett. **11**, 112 (2004).
- [56] A. Stroer et al., "Methods for Detection and Characterization of Signals in Noisy Data with the Hilbert-Huang Transform," Phys. Rev. **D79**, 1s24022 (2009).
- [57] A. Stroer, L. Blackburn and J. Camp, "Comparison of Signals from Gravitational Wave Detectors with Instantaneous Time-Frequency Maps," Class. Quantum Grav. **28**, 155001 (2011).
- [58] H. Takahashi et al., "On Investigating EMD Parameters to Search for Gravitational Waves," Adv. Adapt. Data Anal. **5** 1350010 (2013).
- [59] L. Cohen and C. Lee, Instantaneous Frequency, its Standard Deviation and Multicomponent Signals, Proc. SPIE vol 975, Adv. Algorithms and Arch. For Sig. Proc. III (1988) 186.
- [60] L. Cohen, Instantaneous Bandwidth for Signals and Spectrograms, Proc. IEEE ICASSP-90, vol. 5, 2451.
- [61] P.J. Loughlin and K.L. Davidson, Modified Cohen-Lee Time-Frequency Distributions and Instantaneous Bandwidth of Multicomponent Signals, IEEE Trans Sig. Proc., **49** (2001) 1153.
- [62] B. Picinbono, "On Instantaneous Amplitude and Phase of Signals," IEEE Trans. **45**, 552 (1997).
- [63] G.R. Putland and B. Boashash. "Can a Signal be both Monocomponent and Multicomponent?" in Proc. WoSPA 2000, p. 14 (2000).
- [64] E. Bedrosian, The Analytic Signal Representation of Modulated Waveforms, Proc. IRE, **50**, 2071 (1962).
- [65] E. Bedrosian, A Product Theorem for Hilbert Transforms, Proc. IEEE **51**, 868 (1963).
- [66] A.H. Nuttall, On the Quadrature Approximation to the Hilbert Transform of Modulated Signals, Proc. of the of IEEE **54** (1966) 1458.
- [67] I. Daubechies, L. Jianfeng and H.-T. Wu, "Synchrosqueezed Wavelet Transforms: an Empirical Mode Decomposition-like Tool," Appl. Comput. Harmon. Anal. **30** 243 (2011).
- [68] S. Meignen and V. Perrier, "A New Formulation for Empirical Mode Decomposition Based on Constrained Optimization," IEEE Sig. Proc. Lett., **14**, 932 (2007).
- [69] Z. Wu and N. Huang, "Ensemble Empirical Mode Decomposition: a Noise-Assisted Data Analysis Method," Advances in Adaptive Data Analysis, **1**, 1(2009).
- [70] S. Olhede and A.T. Walden, "The Hilbert Spectrum via Wavelet Projection," Proc. Roy. Soc. Lond. **A460**, 955 (2004).
- [71] X. Fang, H. Luo, "An Improved Hilbert Transform for Nonlinear Vibration Signal Analysis," Proc. 50th AIAA/ASME/ASCE/AHS/ASC Conference, 2651 (2009).
- [72] R.T. Rato, M.D. Ortiguera and A.G. Batista, "On the HHT, its Problems, and Some Solutions," Mechanical Systems and Signal Processing, **22**, 1374 (2008).
- [73] P. Flandrin, "One or Two Frequencies? The Empirical Mode Decomposition Answers," IEEE Trans. Signal Proc. **56**, 85 (2008).
- [74] In (G. Rilling and P. Flandrin, Adv. Adapt. Data Anal. **1**, 43 (2009).) it was further noted that even for a *single-tone* signal, the frequency EMD estimation error blows up with the square of the carrier frequency, and can be small only if the ratio between the sampling and signal frequency is an even integer.
- [75] R. Gupta et al., Estimation of Instantaneous Frequencies Using Iterative Empirical Mode Decomposition, Signal, Image and Video Proc., **8** (2014) 799.
- [76] N.J. Stevenson, M. Mesbah and B. Boashash, "Multiple-View TimeFrequency Distribution Based on the Empirical Mode Decomposition," IET Signal Proc. **4**, 447 (2010).
- [77] S. Mallat and Z. Zhang, "Matching Pursuits with Time-Frequency Dictionaries," IEEE Trans. Signal Process. **41**, 3397 (1993).
- [78] D. Gabor, "Theory of Communication," J. IEE, **93** (1946) 429.
- [79] J.M. Bastiaans, "Gabor's Expansion of a Signal into Gaussian Elementary Signals," Proc. IEEE **68** (1980) 538.
- [80] T.B. Littenberg and N.J. Cornish, "Separating Gravitational Wave Signals from Instrument Artifacts," Phys. Rev. **D82**, 103007 (2010).
- [81] N.J. Cornish and T.B. Littenberg, "Bayeswave: Bayesian Inference for Gravitational Wave Bursts and Instrument Glitches," Class. Quantum Grav. **32** , 135012 (2015).
- [82] B. Abbot et al., "Search for Gravitational Waves Associated with 39 Gamma-Ray Bursts using Data from the Second, Third, and Fourth LIGO Runs," Phys. Rev. **D 77**, 062004 (2008).
- [83] M. M. Goodwin and M. Vetterli, "Matching Pursuit and Atomic Signal Models Based on Recursive Filter Banks," IEEE Trans. Signal Proc. **SP- 47**, 1890 (1999).

- [84] M. G. Christensen and S. van de Par, "Efficient Parametric Coding of Transients.", IEEE Trans. Audio, Speech and Lang. Proc., **14**, 1340 (2006).
- [85] B.L. Sturm and J.J. Shynk, "Sparse Approximation and the Pursuit of Meaningful Signal Models With Interference Adaptation," IEEE Trans. Audio, Speech, Lang. Proc. **19**, 421 (2009).
- [86] B. L. Sturm et al., "Dark Energy in Sparse Atomic Estimations," IEEE Trans. Audio, Speech and Lang. Proc. **16**, 671 (2008).
- [87] B.L. Sturm, J.J. Shynk and D.H. Kim, "Pruning Sparse Signal Models Using Interference," Proc. IEEE CISS'09, p. 454 (2009).
- [88] B.L. Sturm and J.J. Shynk, "Interference-Driven Adaptation in Sparse Approximation," Proc. 42nd Asilomar Conference on Signals, Systems and Computers, p. 241 (2008).
- [89] S. Rampone et al., "Neural Network Aided Glitch-Burst Discrimination and Glitch Classification," International Journal of Modern Physics **C24** (2013) 1350084
- [90] The isotropic Ω domain in the discrete TF plane is a rectangle whose aspect ratio depends on the chosen time-window width and sampling frequency.
- [91] P. Flandrin and P. Borgnat, "Time-Frequency Energy Distributions Meet Compressed Sensing," IEEE Trans. **SP-58** (2010) 2974.
- [92] D. L. Donoho, "Compressed Sensing," IEEE Trans., **IT-52** (2006) 1289.
- [93] E. Candès, J. Romberg and T. Tao, "Robust Uncertainty Principles: Exact Signal Reconstruction from Highly Incomplete Frequency Information," IEEE Trans. Inf. Th., **IT-52** (2006) 489.
- [94] E. Candès, and J. Romberg, " ℓ_1 -MAGIC: Recovery of Sparse Signals via Convex Programming," MATLAB toolbox available online at <http://www-stat.stanford.edu/~candes/l1magic/>.
- [95] S.S. Chen S.S. Chen, D.L. Donoho and M.A. Saunders, "Atomic Decomposition by Basis Pursuit," SIAM Rev., **43** (2001) 129.
- [96] D.L. Donoho, M Elad, and V.N. Temlyakov, "Stable Recovery of Sparse Overcomplete Representations in the Presence of Noise," IEEE Trans. **IT-52** (2006) 6.
- [97] R.T. Rockafellar, "*Convex Analysis*," Princeton University Press, Princeton NJ (1970).
- [98] M.A.T. Figueiredo, R. Nowak and S.J. Wright "Gradient Projection for Sparse Reconstruction: Application to Compressed Sensing and Other Inverse Problems," IEEE J. Sel. Top. Sig. Proc., **1** (2007) 586.
- [99] For $\text{card}[\Omega_0] \sim N$, the L_1 distance between the actual and constructed skeleton was minimized, and the Renyi entropy of \widehat{W} reproduced that of the *actual* skeleton..
- [100] B. Jokanovic et al., "Time-Frequency Kernel Design for Sparse Joint-Variable Signal Representations," Proc. 22nd European Signal Proc. Conf. (EUSIPCO 2014), p. 2100.
- [101] The radial Gaussian Kernel toolbox is available from <http://www.ece.rice.edu/dsp/software/rgk.shtml>
- [102] The GPSR toolbox is available from www.lx.it.pt/~mtf/GPSR under the GNU License.
- [103] The Q-Transform toolbox is available from <http://www.ligo.caltech.edu/~shourov/q/qscan/code/qscan/src/>
- [104] L. Cohen, "What is a Multicomponent Signal," Proc. ICASSP '92 (5) p. 113.
- [105] A.E. Barnes, The Calculation of Instantaneous Frequency and Instantaneous Bandwidth, Geophys. **57** (1992) 1520.
- [106] P. Saulson, "Listening to Glitches," LIGO document G070548 (2007) and related project web-pages at http://physics.syr.edu/research/relativity/ligo/restricted/glitch_catalog/ .
- [107] A. Fusco et al., "An Atlas of Compressed Coding Retrieved LIGO S5 Glitch Skeletons," LIGO document T1300598. (2013).
- [108] M. Was, private communication (2013).

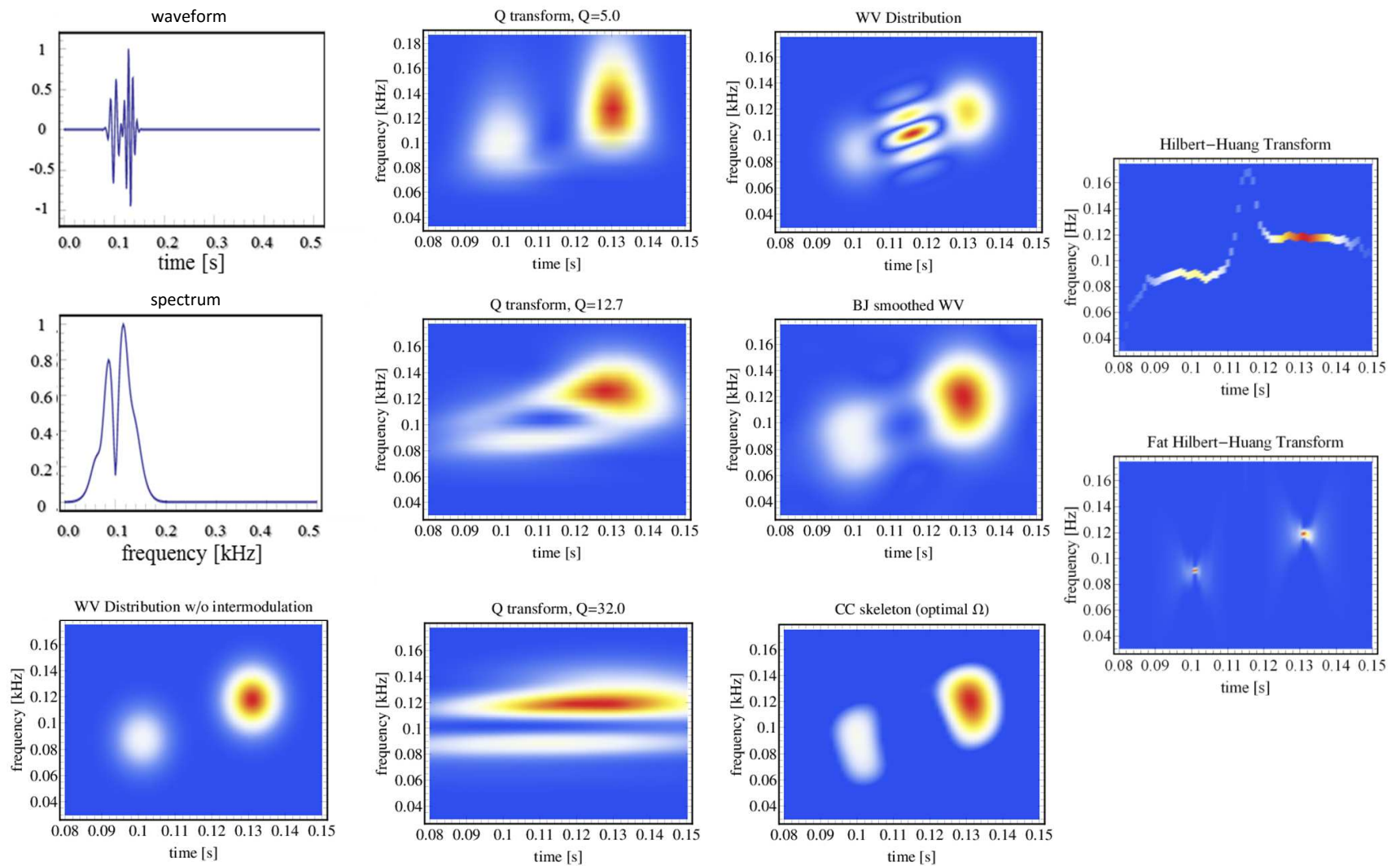


Figure 2 – Gabor molecule consisting of two atoms with different time centroids and carrier frequencies. Comparison among the Q transform, the Wigner-Ville (plain, BJ-smoothed and CC cured), and the Hilbert-Huang transform without and with (fat) IBW information.

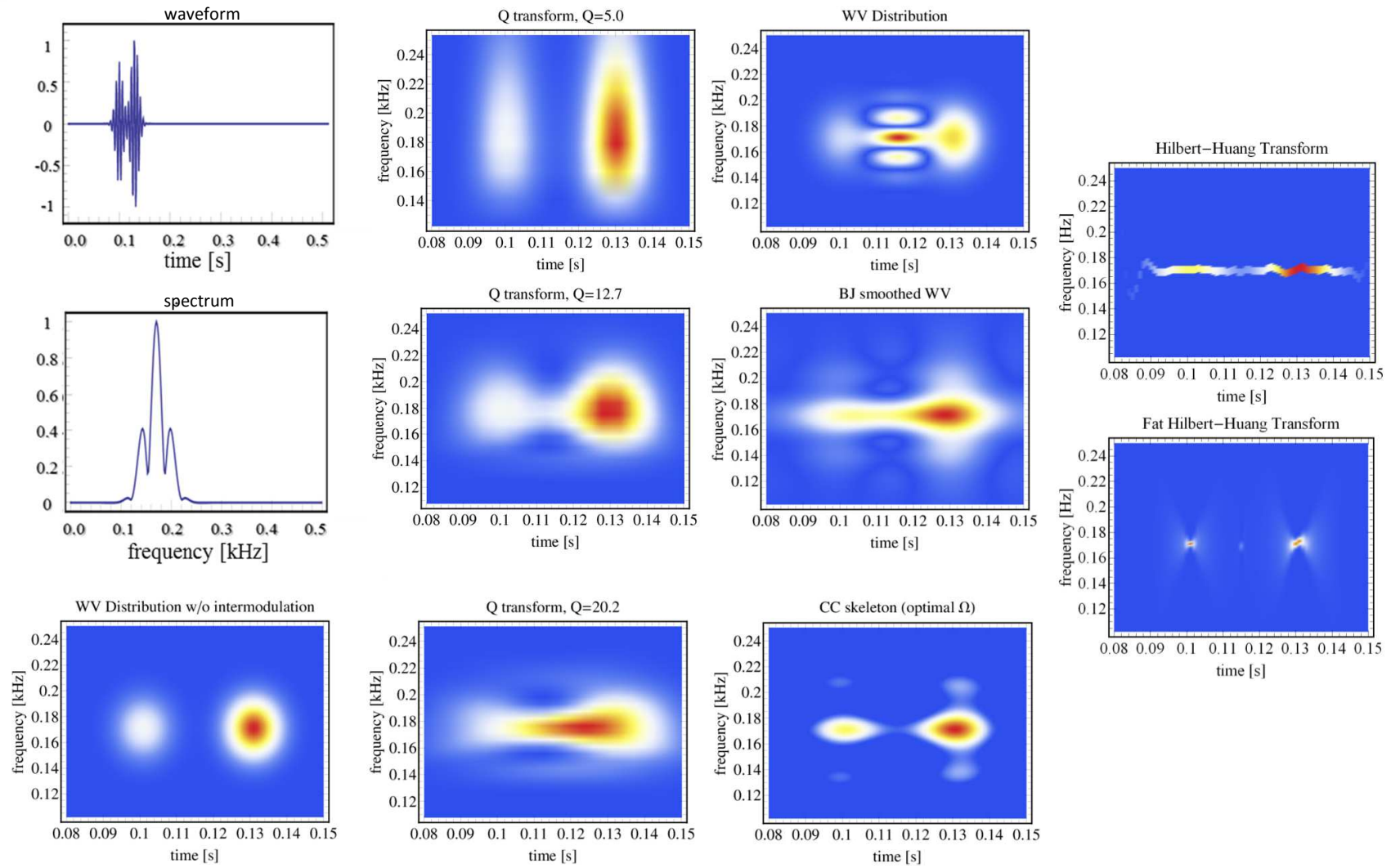


Figure 3 – Gabor molecule consisting of two atoms with different time centroids and equal carrier frequencies. Comparison among the Q transform, the Wigner-Ville (plain, BJ-smoothed and CC cured), and the Hilbert-Huang transform without and with (fat) IBW information.

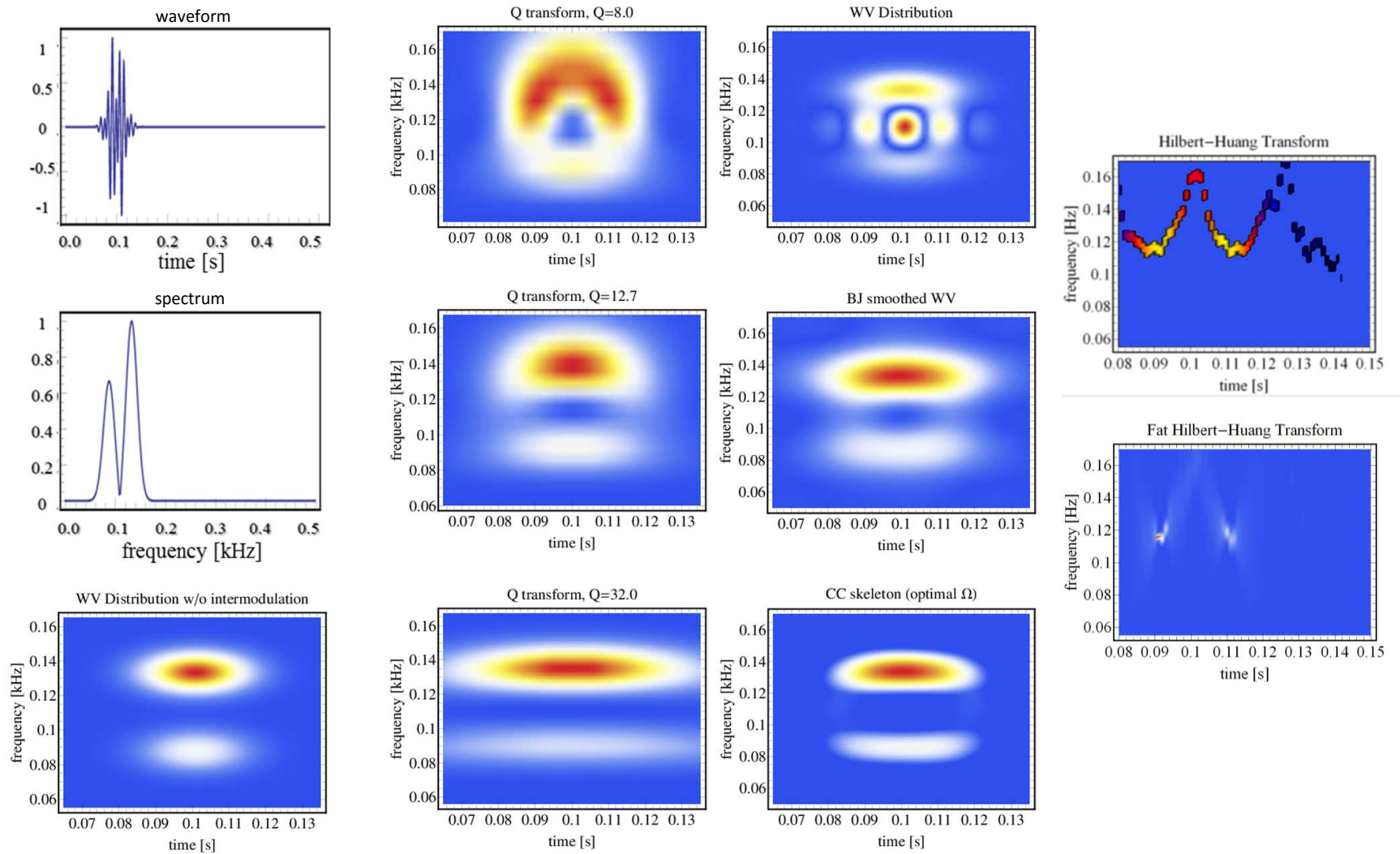


Figure 4 – Gabor molecule consisting of two atoms with equal time centroids and different carrier frequencies. Comparison among the Q transform, the Wigner-Ville (plain, BJ-smooth-ed and CC cured), and the Hilbert-Huang transform without and with (fat) IBW information.

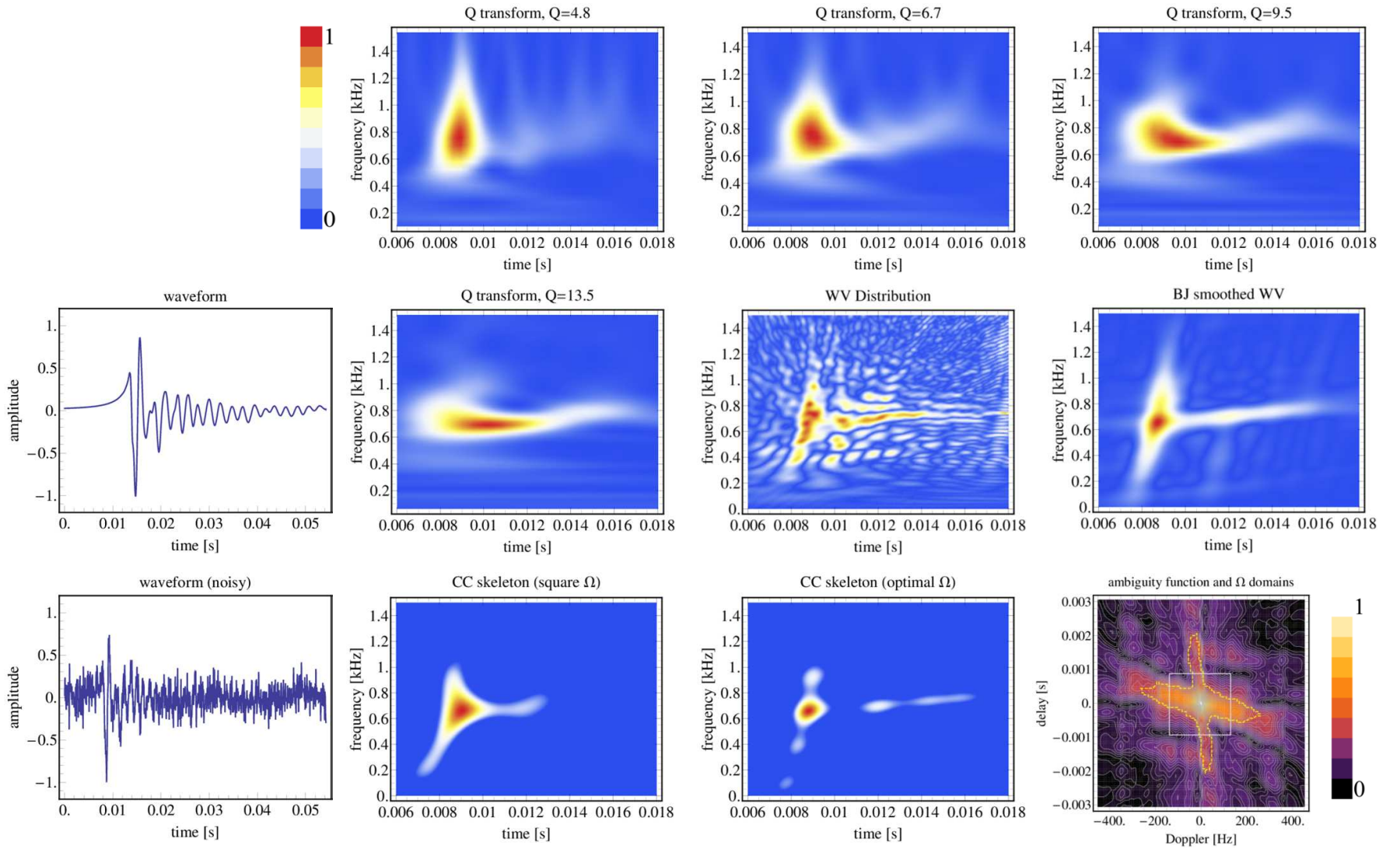


Figure 5 - Supernova core-collapse GW waveform from [31]. The panels display the time waveform (noise-free and with added white Gaussian noise), the Q-transforms for $Q=4.8$, 6.7 , 9.5 , and 13.5 , the WV and the BJ-smoothed WV, the CC skeletons obtained using the square and BJ-optimized Ω domain, and the pertinent ambiguity function, together with the square and BJ-optimized Ω domain boundaries.

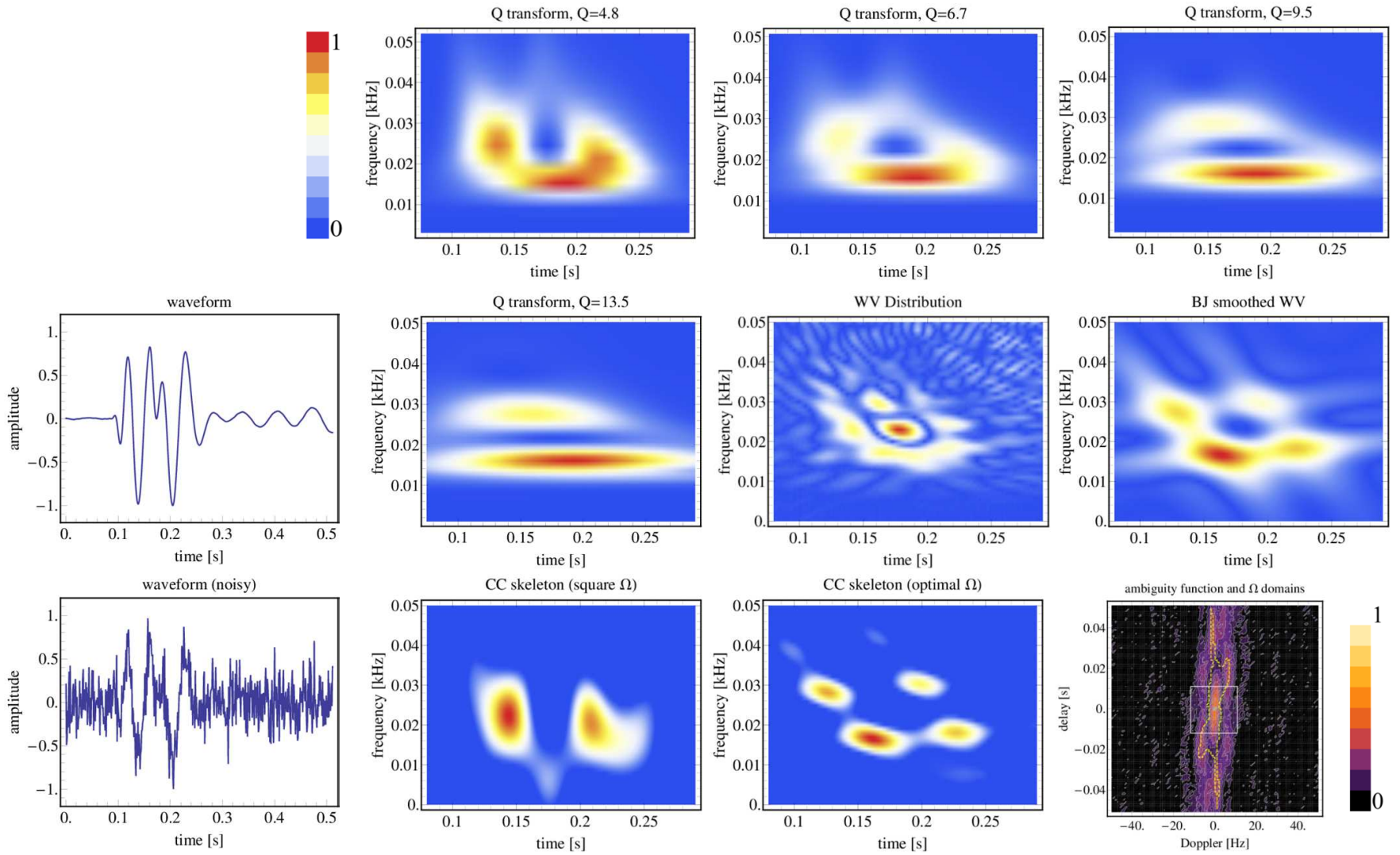


Figure 6a - A LIGO glitch from the 5th Science Run (part of H1 DARM_ERR_866273637 from [51]). The panels display the time waveform (noise-free and with added white Gaussian noise), the Q-transforms for $Q=4.8$, 6.7 , 9.5 , and 13.5 , the WV and the BJ-smoothed WV, the CC skeletons obtained using the square and BJ-optimized Ω domain, and the pertinent ambiguity function, together with the square and BJ-optimized Ω domain boundaries.

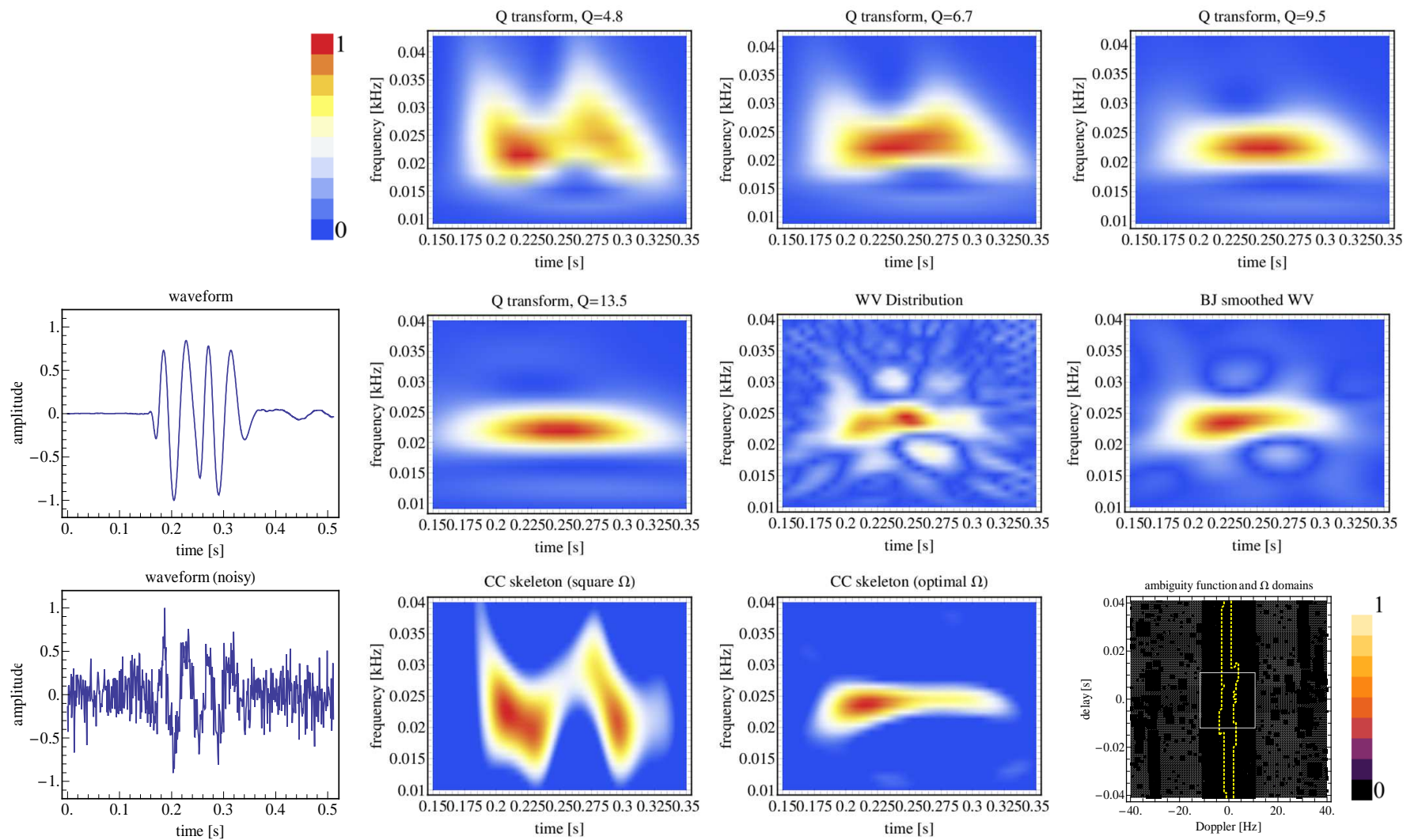


Figure 6b - A LIGO (power_mag) glitch from the 5th Science Run from [51]. The panels display the time wave-form (noise-free and with added white Gaussian noise), the Q-transforms for $Q=4.8$, 6.7 , 9.5 , and 13.5 , the WV and the BJ-smoothed WV, the CC skeletons obtained using the square and BJ-optimized Ω domain, and the pertinent ambiguity functions, together with the square and BJ-optimized Ω domain boundaries.

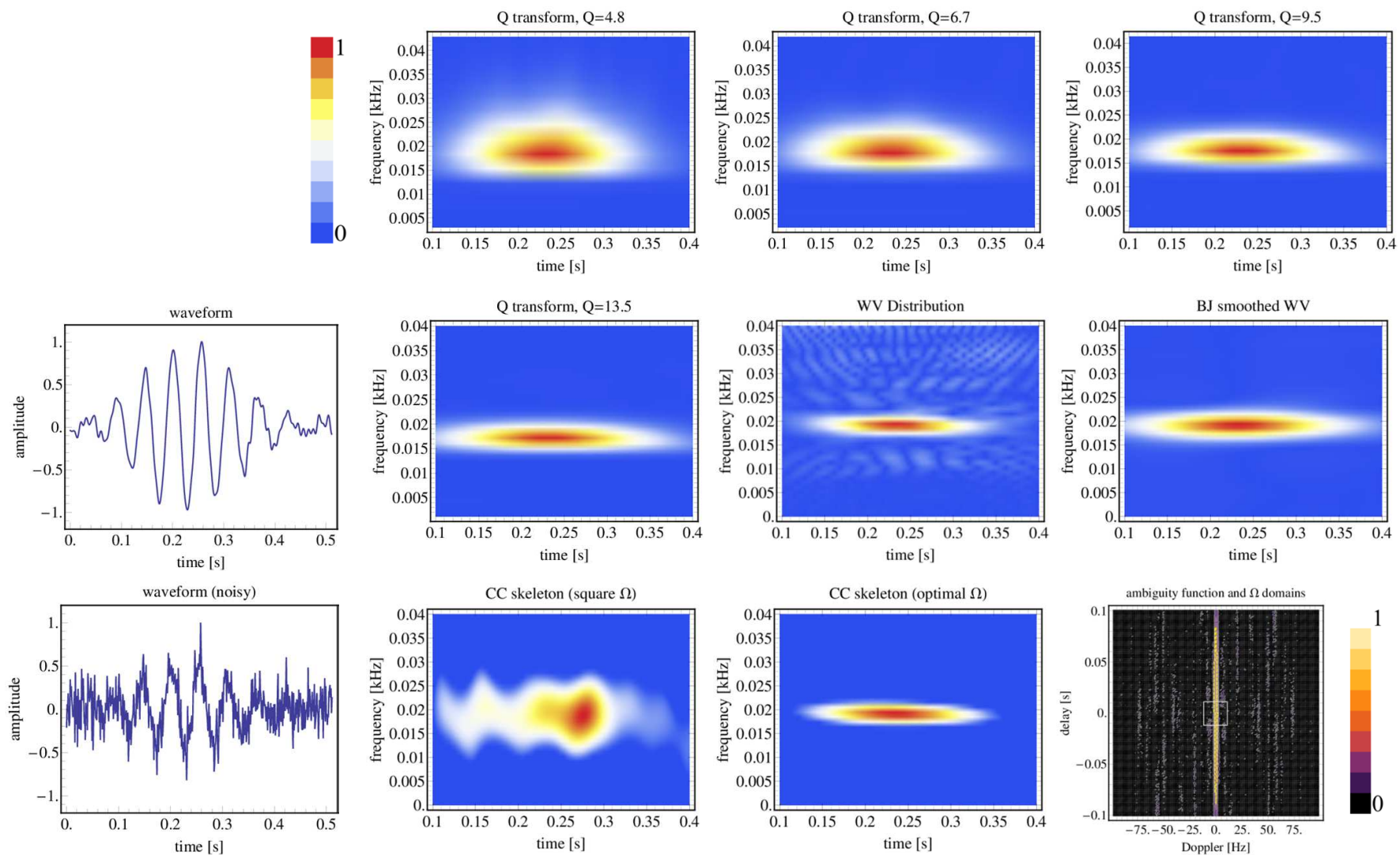


Figure 6c - A LIGO (power_mag) glitch from the 5th Science Run from [51]. The panels display the time wave-form (noise-free and with added white Gaussian noise), the Q-transforms for $Q=4.8$, 6.7 , 9.5 , and 13.5 , the WV and the BJ-smoothed WV, the CC skeletons obtained using the square and BJ-optimized Ω domain, and the pertinent ambiguity function, together with the square and BJ-optimized Ω domain boundaries.

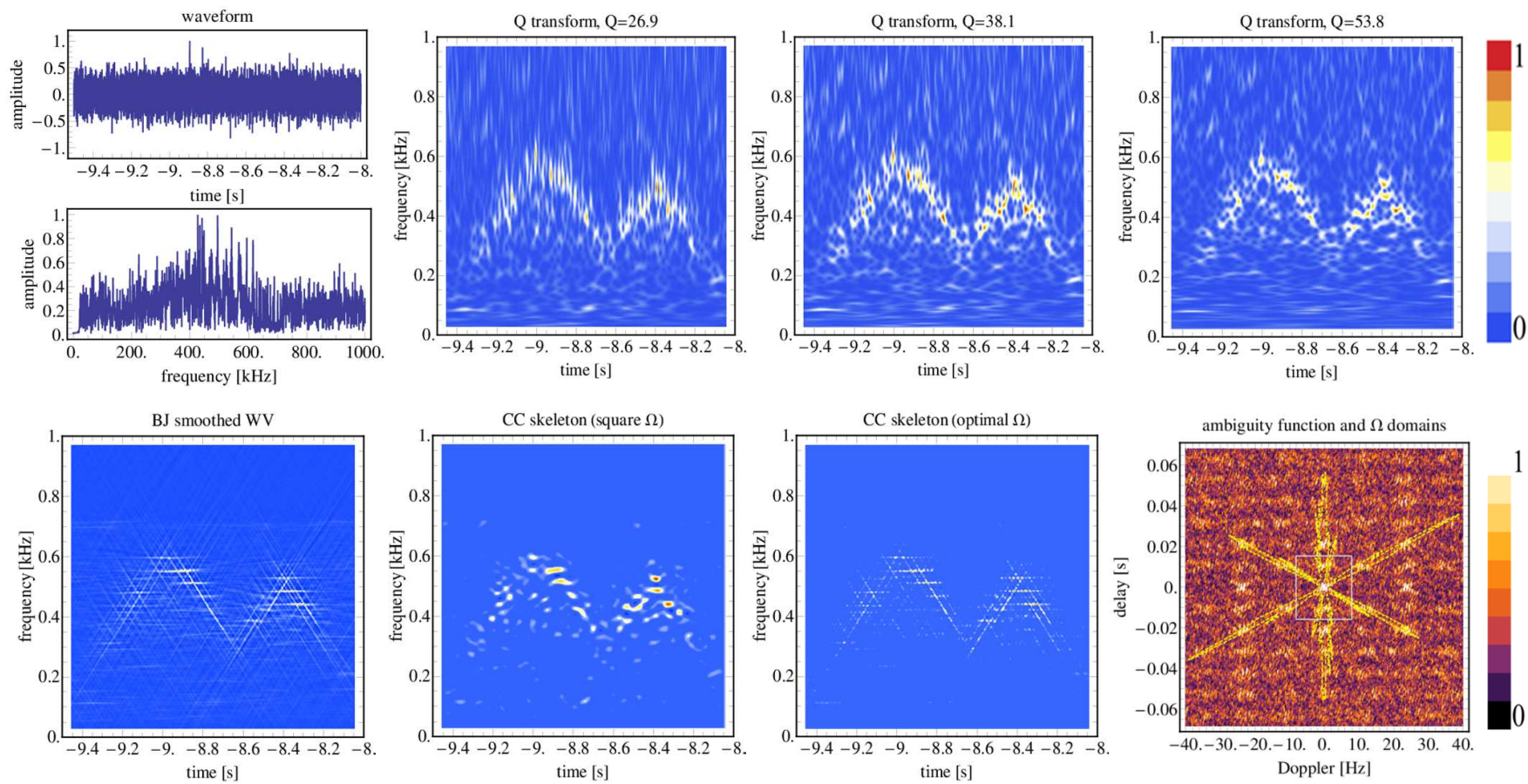


Figure 7 - A GEO-600 arch-glitch [51]. The panels display the (noisy) waveform and its frequency spectrum, the Q-transforms for $Q=26.9$, 38.1 and 53.8 , the BJ-smoothed WV, the CC skeletons obtained using the square and BJ-optimized Ω domain, and the pertinent ambiguity function, together with the square and BJ-optimized Ω domain boundaries.

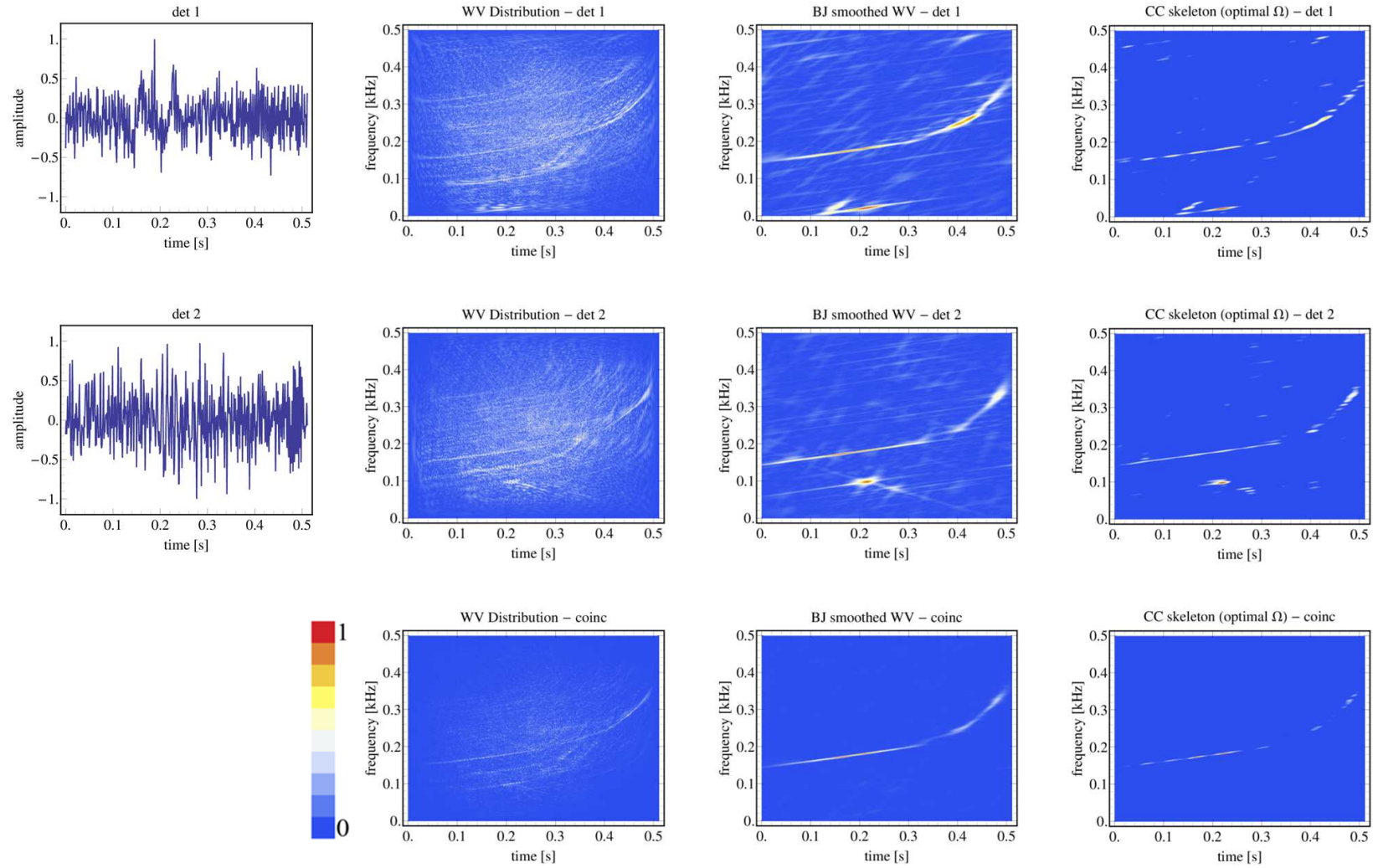


Figure 8a - TF Consistency tests (triggered search, incoherent detection) between two detectors, eq. (24). The panels display the waveforms and the WV, BJ-smoothed WV, and CC skeleton with BJ-optimized Ω domain. The data in each detector include a Newtonian GW chirp with SNR=15 against the additive white Gaussian background, and a random SG-glitch, with SNR=7.5.

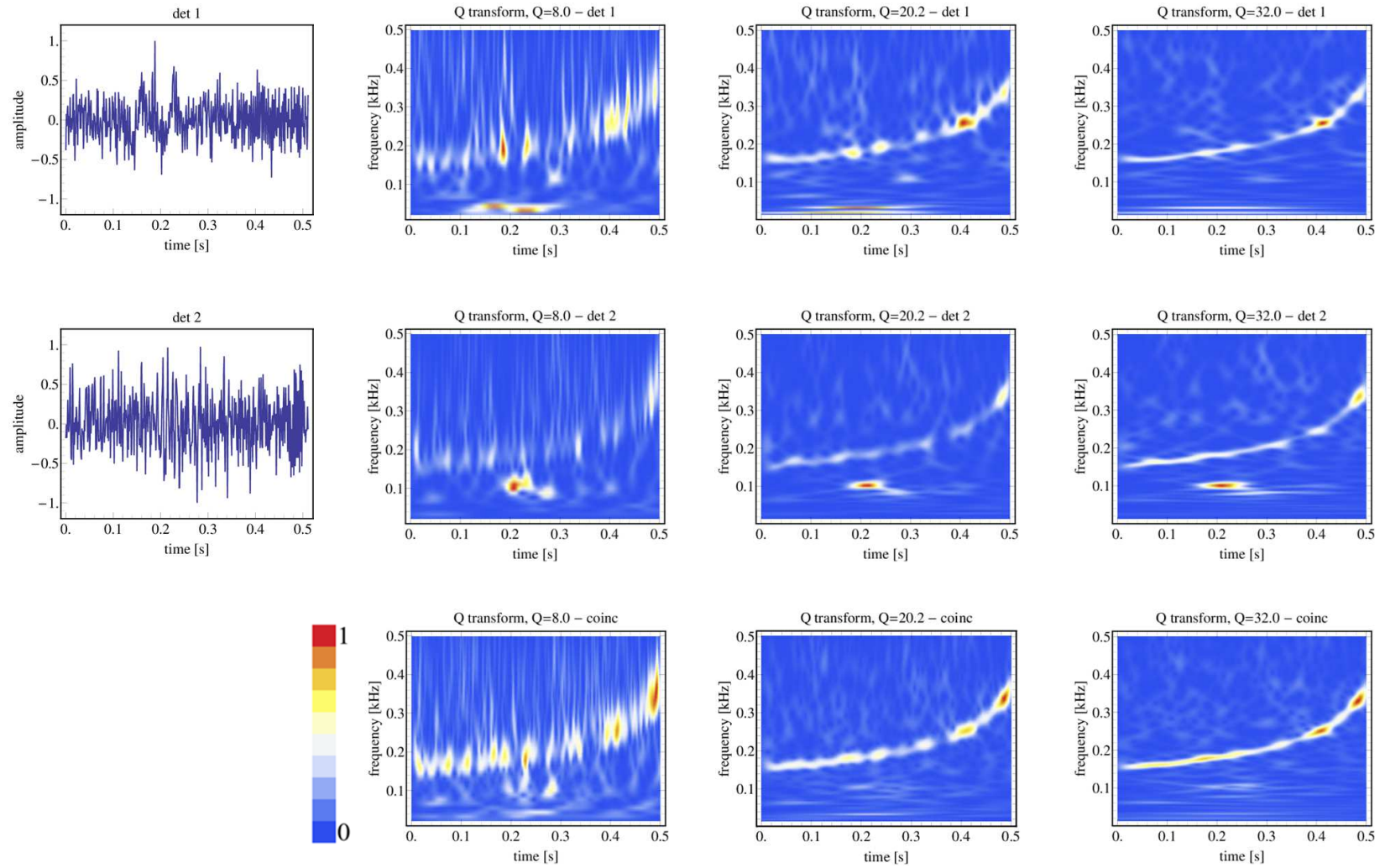


Figure 8b - TF Consistency tests (triggered search, incoherent detection) between two detectors, eq. (24). The panels display the waveforms and the Q-transforms with $Q=8$, 20.2 and 32. The data in each detector are the same as in Fig.5a, and include a Newtonian GW chirp with $\text{SNR}=15$ against the additive white Gaussian background, and a random SG-glitch, with $\text{SNR}=7.5$.

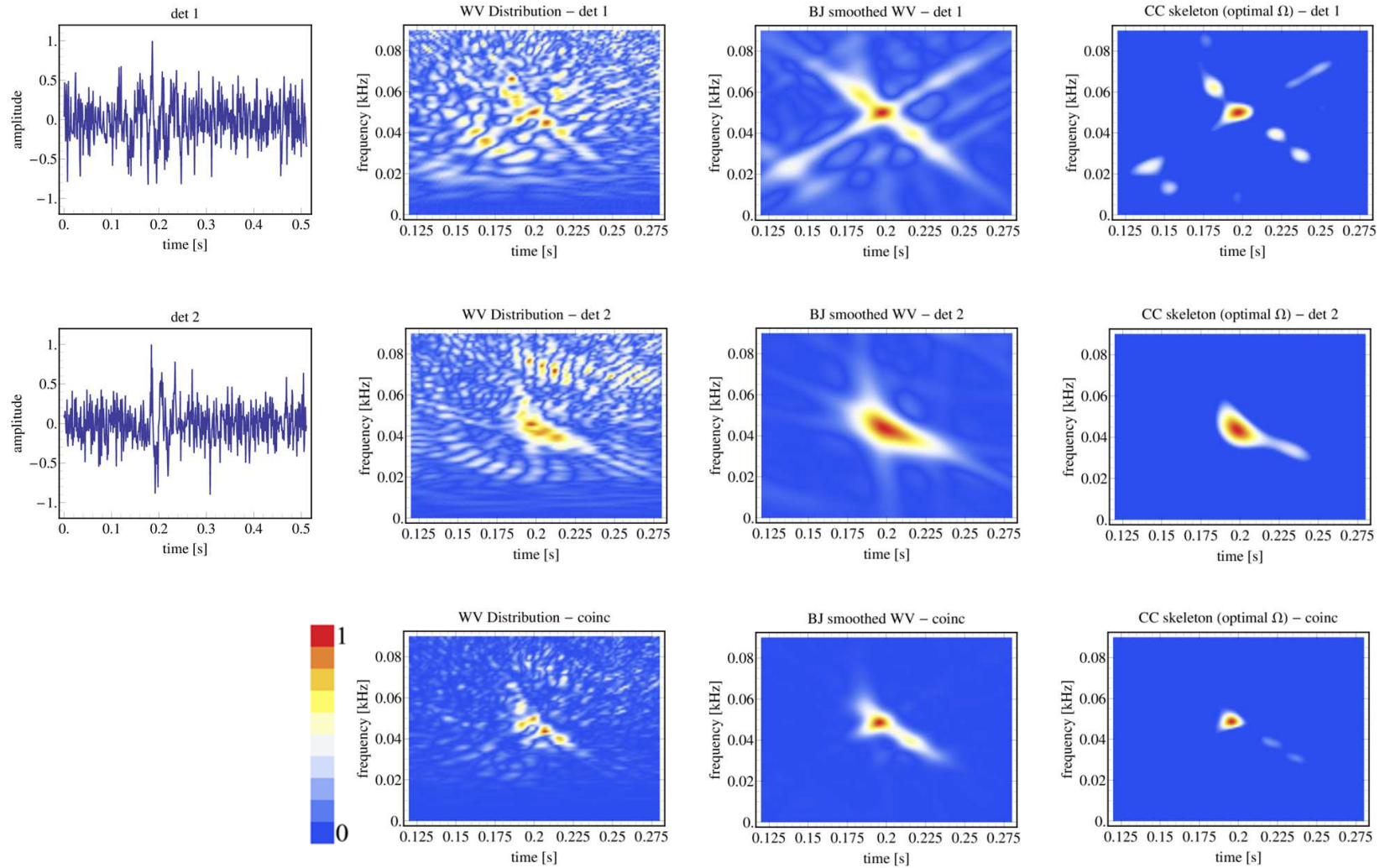


Figure 8c - TF Consistency tests (triggered search, incoherent detection) between two detectors, eq. (24). The panels display the Waveforms and the WV, BJ-smoothed WV, and CC skeleton with BJ-optimized Ω domain. The data in each detector include a GW merger from [30] with SNR=10 against the additive white Gaussian background, and a random SG-glitch, with SNR=5.

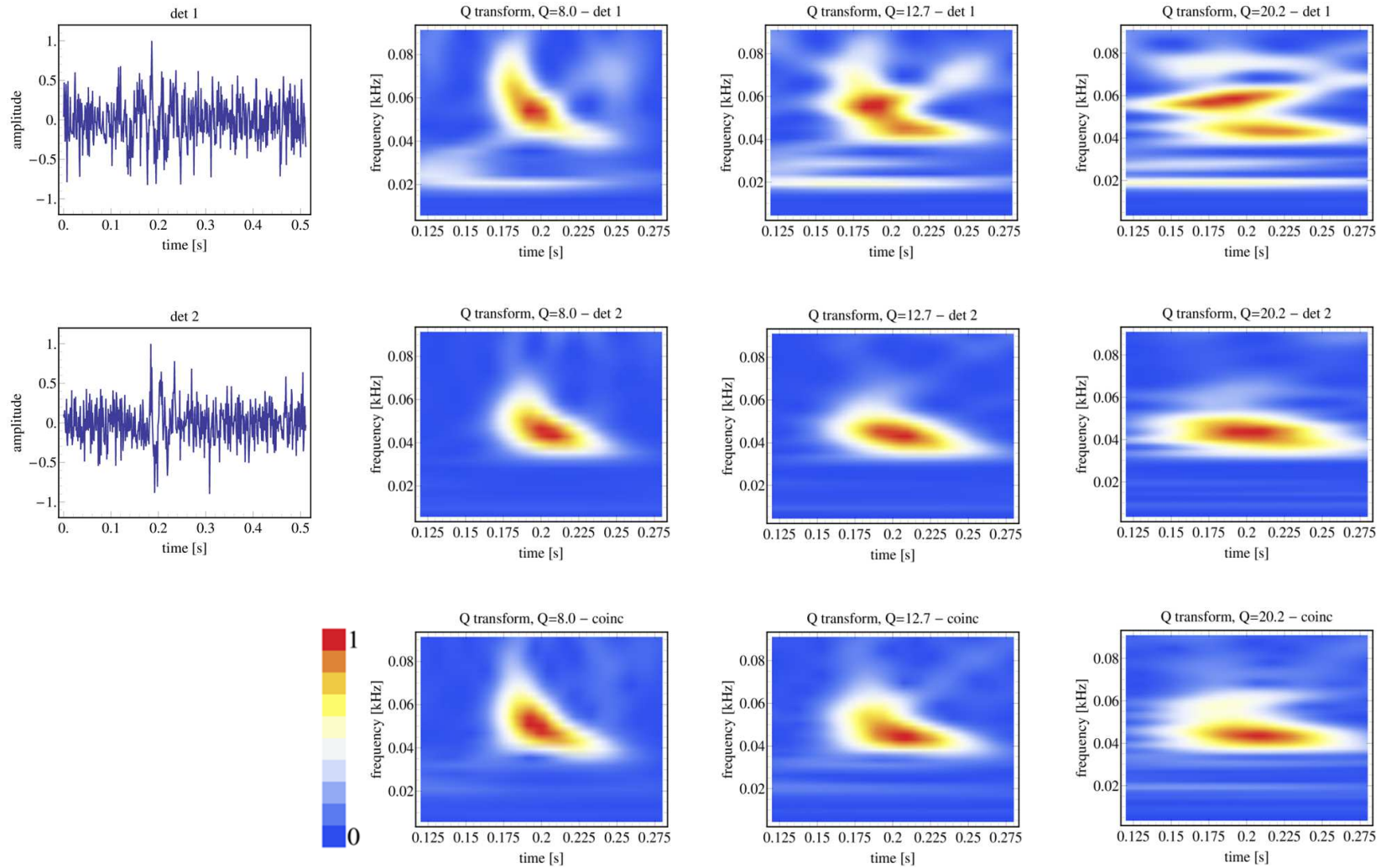


Figure 8d - TF Consistency tests (triggered search, incoherent detection) between two detectors, eq. (24). The panels display the waveforms and the Q-transforms with $Q=8$, 20.2 and 32. The data in each detector are the same as in Fig.5c, and include a GW merger from [30] with $\text{SNR}=10$ against the additive white Gaussian background, and a random SG-glitch, with $\text{SNR}=5$.

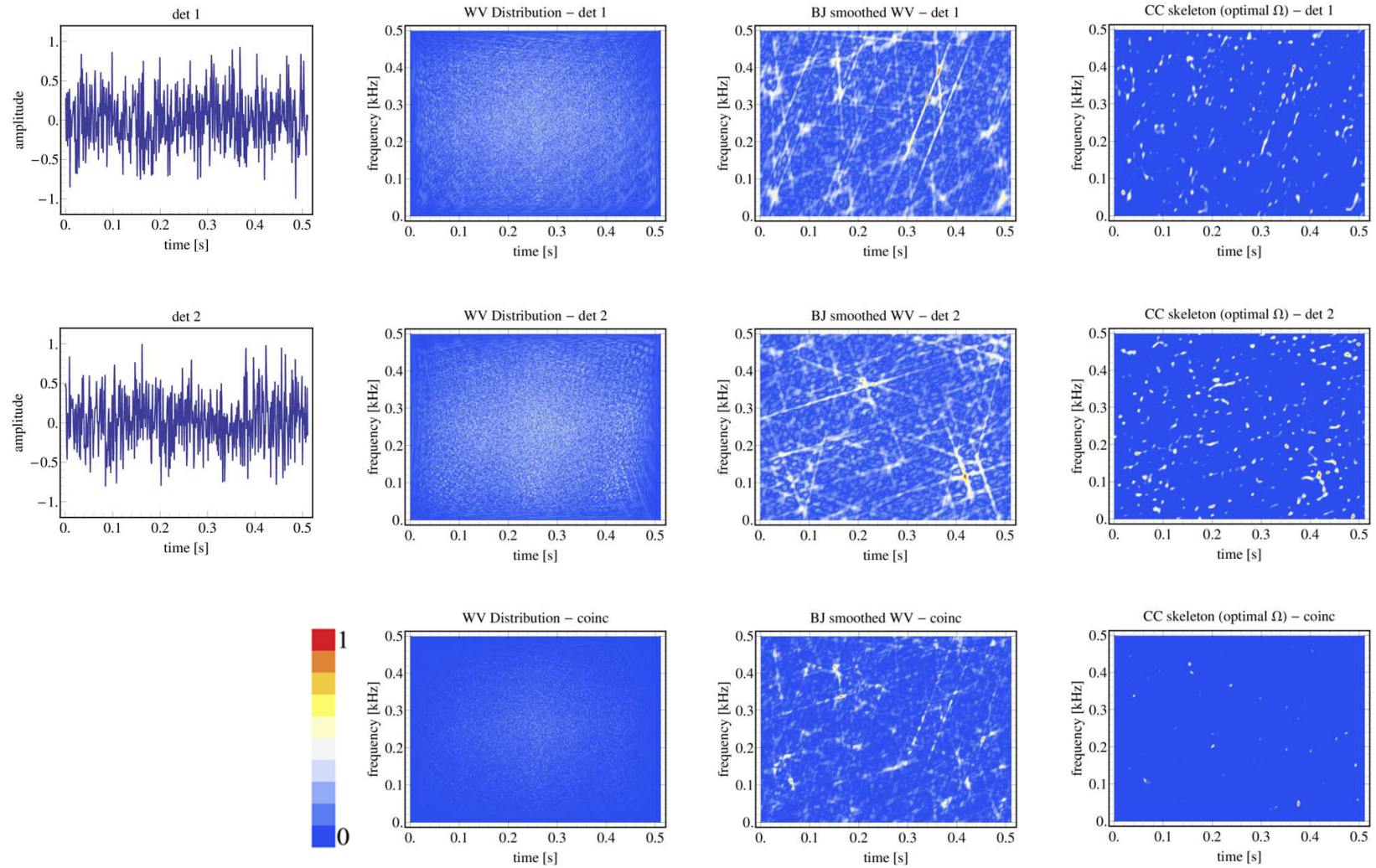


Figure 8e - TF Consistency test (triggered search, incoherent detection) between two detectors, eq. (24). The panels display the waveforms and the WV, BJ-smoothed WV, and CC skeleton with BJ-optimized Ω domain. The data in each detector consist of independent realizations of white Gaussian noise with the same power spectral density as the background noise in Fig.s 5a-5d.

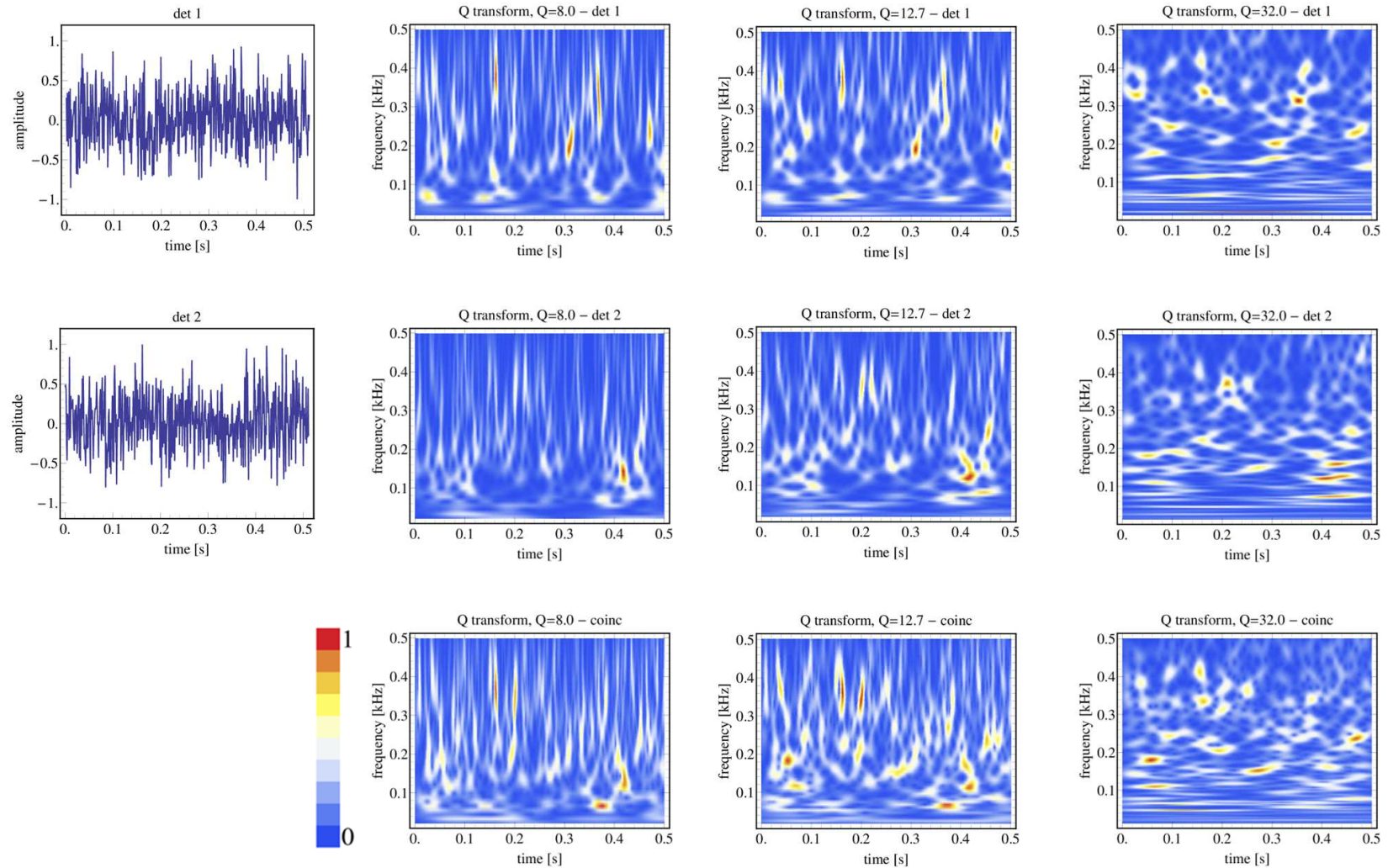


Figure 8f - TF Consistency tests (triggered search, incoherent detection) between two detectors, eq. (24). The panels display the waveforms and the Q-transforms with $Q=8$, 12.7 and 32. The data in each detector consist of independent realizations of white Gaussian noise with the same power spectral density as the background noise in Fig.s 5a-5d.

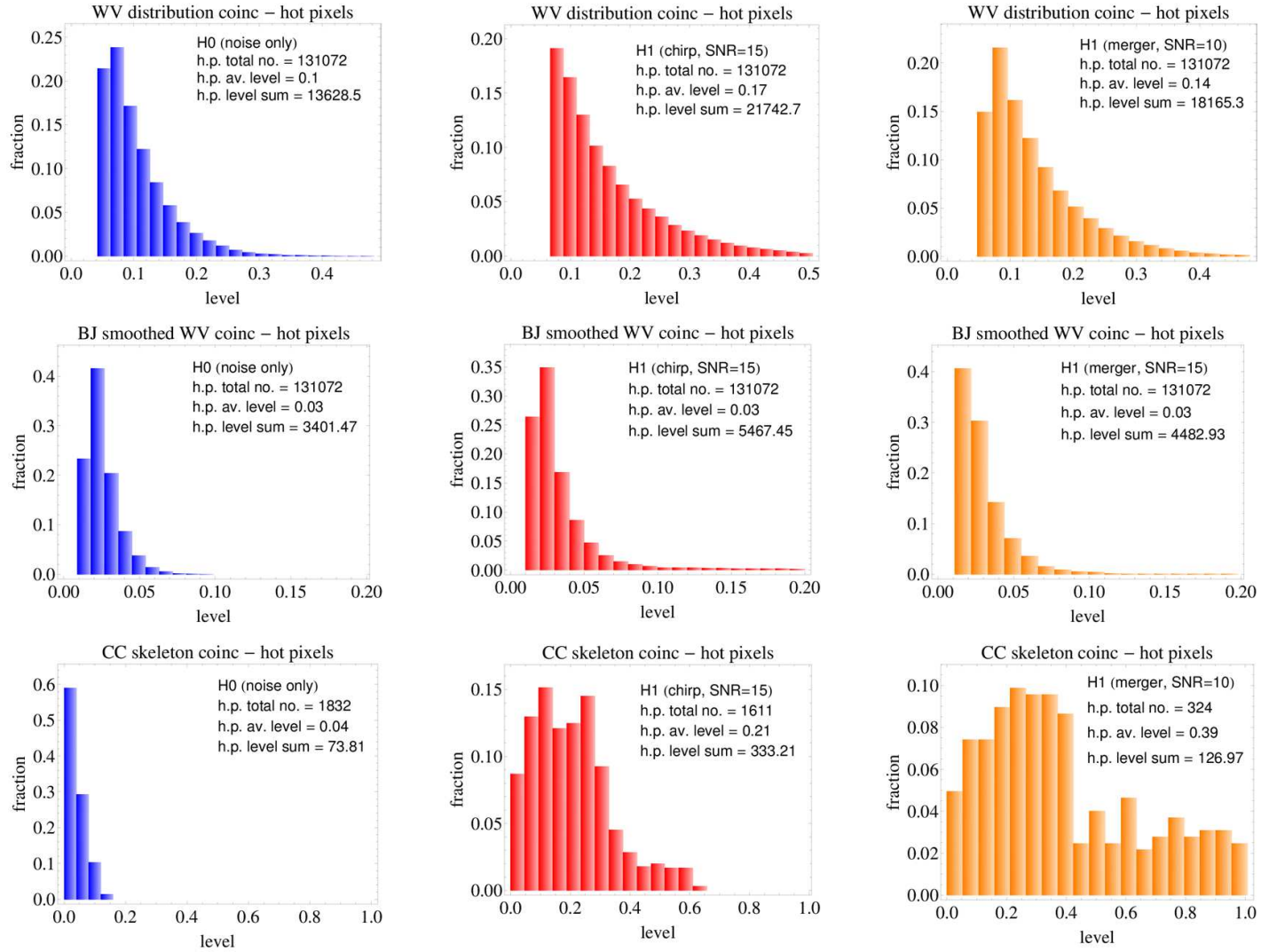


Figure 9a - TF Consistency tests (triggered search, incoherent detection) between two detectors. WV, BJ-smoothed WV, and CC skeleton with BJ-optimized domain. Level histograms of the hot pixels in the coincidence distributions.

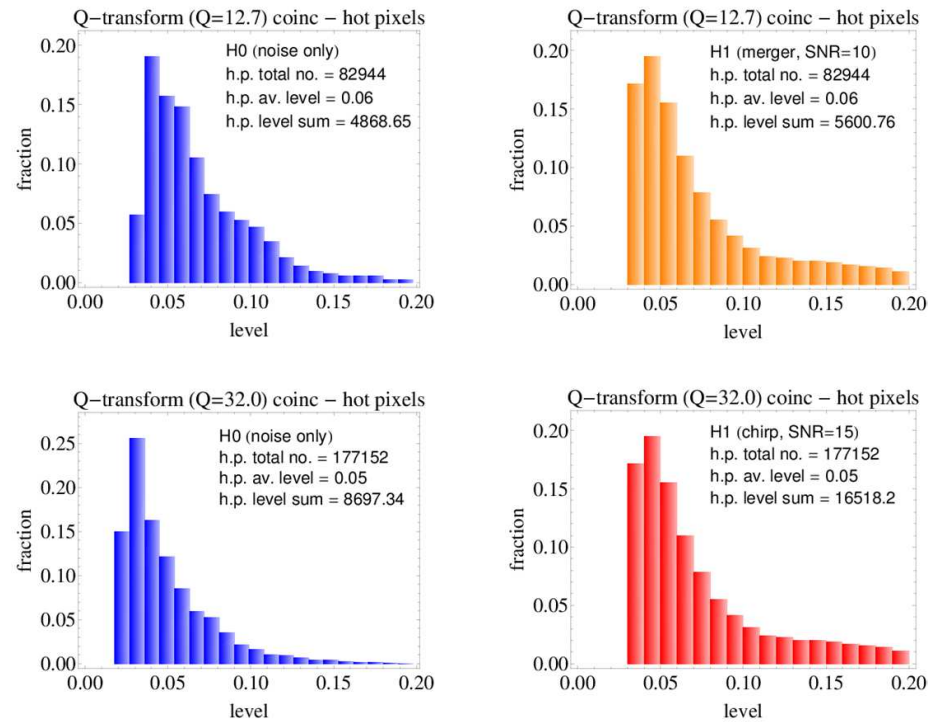


Figure 9b - TF Consistency tests (triggered search, incoherent detection) between two detectors. Q transforms with Q=12.7 (GW merger, SNR=10) and Q=32 (GW chirp, SNR=15). Level histograms of the hot pixels in the coincidence distributions.

